

1 **Sex-specific chromatin remodelling safeguards transcription in germ cells**

2

3 **Tien-Chi Huang^{1,2}, Yi-Fang Wang^{1*}, Eric Vazquez-Ferrer^{1,2*}, Cristina E. Requena^{1,2}, Courtney**
4 **Hanna^{3,4}, Gavin Kelsey^{3,4} and Petra Hajkova^{1,2 †}**

5

6 ¹MRC London Institute of Medical Sciences (LMS), Du Cane Road, London W12 0NN, UK.

7 ²Institute of Clinical Sciences (ICS), Faculty of Medicine, Imperial College London, Du Cane
8 Road, London, W12 0NN, UK

9 ³Epigenetics Programme, Babraham Institute, Cambridge, UK

10 ⁴Centre for Trophoblast Research, University of Cambridge, Cambridge, UK

11

12 *these authors contributed equally

13

14 †Correspondence: petra.hajkova@lms.mrc.ac.uk

15 Tel: +44 (0)20 83838264

16

17

18

19

20 **Abstract:**

21 Stability of the epigenetic landscape underpins maintenance of the cell type specific transcriptional
22 profile. DNA methylation as one of the main repressive epigenetic systems has been shown to be
23 important for long term gene silencing; its loss leading to ectopic and aberrant transcription in
24 differentiated cells and cancer¹. Interestingly, the developing mouse germ line endures global
25 changes in DNA methylation in the absence of widespread transcriptional activation. Using an ultra-
26 low input native (ULI-n) CHIP approach we show that following DNA demethylation the gonadal
27 primordial germ cells (PGCs) undergo remodelling of repressive histone modifications resulting in a
28 sex specific signature. We further demonstrate that polycomb plays a central role in transcriptional
29 control in the newly hypomethylated germline genome as the genetic loss of *Ezh2* leads to aberrant
30 transcriptional activation, retrotransposon derepression and dramatic loss of developing female
31 germ cells. Last but not least, we show that the base composition of promoters determines
32 H3K27me3 enrichment following the loss of DNA methylation. Overall, our study provides
33 unprecedented insight into the dynamic interplay between repressive chromatin modifications in
34 the context of a developmental reprogramming system.

35

36

37 DNA methylation is functionally associated with transcriptional silencing of tissue-specific genes and
38 repression of transposable elements (TEs). Although globally relatively stable in the soma,
39 development of the mammalian germ line is associated with profound changes in genomic DNA
40 methylation²⁻⁴. Following the specification of nascent primordial germ cells (PGCs) at embryonic day
41 E6.25 in the mouse, global changes in the germline epigenome encompass both reprogramming of
42 histone modifications as well as erosion of genome-wide DNA methylation^{5,6}. Global DNA
43 methylation drops gradually during germ cell migration and further decreases extensively between
44 E10.5 and E12.5 once PGCs have entered the genital ridge, installing the most hypomethylated state
45 ever observed during normal development⁷. The gonadal reprogramming directly precedes sex
46 differentiation followed by the onset of meiosis in female PGCs and proliferation arrest in the male
47 germ line⁸ (Fig. 1a).

48 Several lines of evidence indicate that the loss of DNA methylation and TET1-mediated
49 transcriptional activation are crucial for the initiation of the expression of key germline genes at this
50 developmental stage⁹. However, the molecular mechanisms that enable germ cells to maintain and
51 co-ordinate the progressive gene activation and prevent precocious or aberrant wide-spread
52 transcription that could be triggered by genome-wide DNA demethylation are unclear.

53 We have previously shown that the global loss of DNA methylation in the gonadal PGCs temporally
54 overlaps with other major changes in chromatin structure and global histone modifications⁶. In
55 order to understand the temporal changes and to address whether remodeling of the
56 heterochromatin silencing could functionally compensate for the global loss of DNA methylation to
57 provide the means of transcriptional control at this critical stage of PGC development we assessed
58 H3K27me3 and H3K9me3 using an ultra-low input native chromatin immunoprecipitation (ULI-
59 nChIP-seq)^{10,11}. The analysis was carried out using 1000 PGCs isolated from E10.5 (pre-gonadal
60 reprogramming) and E13.5 (post-gonadal reprogramming) male and female embryos derived from
61 C57BL/6 X Δ PE-Oct4-GFP crosses¹² (Extended Data Fig.1a, 1b,1c). Similar to previous reports in ES
62 cells¹³, more than 50% of H3K27me3 peaks overlapped with promoters and gene body (Fig. 1b) with
63 30% of H3K27me3 peaks located within 1kb of the transcription start sites (TSS) (Extended Data Fig.
64 1d, 1e). In contrast, 75% of H3K9me3 peaks localised to intergenic regions, remote from the
65 annotated TSSs (Fig. 1b, Extended Data Fig. 1d, 1e) with clear peak enrichment at repetitive
66 sequences (58% at E10.5, 64% in E13.5 female and 68% for E13.5 male, respectively) (Extended Data
67 Fig 1f).

68

69 Our ULI-nChIP Seq analysis revealed relatively low correlation between E13.5 male and female PGCs
70 for both H3K27me3 and H3K9me3 documenting sex specific differences at this stage of germline
71 development (Spearman correlation coefficient 0.43 for H3K27me3, 0.5 for H3K9me3) (Fig 1c).
72 Furthermore, for both H3K9me3 and H3K27me3 the correlation between E10.5 and E13.5 PGC
73 samples is even lower than it is between sexes suggesting that the repressive chromatin is globally
74 remodelled between E10.5 and E13.5 alongside the global wave of DNA demethylation (Fig. 1c). In
75 further support of this notion, the peak number of H3K27me3 was greatly reduced from E10.5 to
76 E13.5 in both male and female germ cells (Fig. 1d). Although the loss of H3K27me3 peaks is more
77 pronounced in male PGCs (6933 peaks in the female PGCs vs 2740 identified peaks in the male PGCs),
78 even female cells had only 40% of the peaks persisting from E10.5 with the majority of peaks being
79 newly generated during the reprogramming process (Fig. 1d). Sex specific re-configuration of the
80 signal is also evident upon analysis of the H3K9me3 signal. Despite the comparable number of
81 enriched loci, H3K9me3 seems to be remodelled in female PGCs between E10.5 and E13.5; while the
82 male specific loss of H3K27me3 peaks described above seems to be compensated by a dramatic (2.7
83 fold) increase in the number of H3K9me3 peaks observed in male E13.5 PGCs (Fig. 1e). Of note, the
84 majority of male H3K9me3 peaks are relatively short, compared with peaks observed at E10.5
85 (Extended Data Fig. 1h). Despite a significant change in peaks number, the average ChIP intensity
86 relative to input within peaks are comparable between stages (Extended Data Fig. 1g). Furthermore,
87 the observed sex specific remodelling of heterochromatin is not underpinned by profound changes
88 in the abundance of relevant histone modifications, or differential expression of the relevant histone
89 methyltransferases (Fig. 1f, Supplementary Table 3); but potentially linked to a difference in
90 targeting of histone modifying complexes. Indeed, we observed sex specific expression of the
91 polycomb repressive complex 2 (PRC2) auxiliary subunits AEBP2 and PHF19, known to be implicated
92 in polycomb targeting (Extended Fig. 6a, 6b)^{14,15}. Collectively, our analysis shows that global loss of
93 DNA methylation in gonadal germ cells coincides with genome-wide reprogramming of repressive
94 histone modifications, resulting in a sex specific heterochromatin configuration in PGCs at E13.5.

95

96 H3K27me3 is catalysed by PRC2 that shows clear preference for binding to unmethylated CG-rich
97 sequences in mammalian cells¹⁶. We thus asked whether the H3K27me3 remodelling observed in
98 PGCs is due to PRC2 recruitment in response to the global loss of DNA methylation. Our whole
99 genome bisulphite sequencing (WGBS) datasets⁹ show that promoter methylation (5mC+5hmC)
100 significantly decreases from E10.5 to E12.5 in both sexes (Extended Data Fig. 2a). However, this does
101 not lead to an overall global increase in H3K27me3 deposition (Extended Data Fig. 2b, 2c).

102 To understand the potential relationship better, we categorised promoters based on the pattern of
103 dynamic changes between DNA methylation and H3K27me3 from E10.5 to E13.5 (See Methods). We
104 observed 4 different patterns: Group A: loss of 5mC, gain of H3K27me3; Group B: loss of 5mC,
105 continuous H3K27me3 enrichment; Group C: devoid of 5mC, continuous high level of H3K27me3;
106 Group D: loss of 5mC, devoid of H3K27me3 (Fig. 2a, Extended Data Fig 3). Of note, all promoters
107 showed general H3K9me3 reduction between E10.5 and E13.5 alongside global DNA demethylation
108 (Extended Data Fig 3a). Promoters showing consistently high H3K27me3 enrichment (Group C) are
109 characterised by high CpG density, high C+G content and lack of DNA methylation at E10.5 (Fig. 2b),
110 consistent with the known characteristics of polycomb targets in mammalian cells¹⁶. Promoters with
111 lower CpG density contain DNA methylation at E10.5 (Groups A, B and D); however, following
112 methylation loss, CpG density and G+C content determine the polycomb recruitment. As an
113 example, both group A and group D lose DNA methylation, but compared with Group A that attracts
114 H3K27me3 (CpG obs/exp ratio=0.27, GC percentage =46.6%), Group D has significantly lower
115 frequency of CpG (CpG obs/exp ratio=0.22) and G+C (44.8%) ($P < 2 \times 10^{-16}$, pairwise Wilcoxon test) (Fig.
116 2b). This suggests that critical threshold of CpG density and G+C enrichment is required to render
117 promoters capable of recruiting PRC2 once DNA methylation is removed (Fig. 2c). Interestingly, this
118 relationship is less obvious in the male E13.5 PGCs (Extended Data Fig. 2d, 2e), suggesting a key role
119 for PRC2 subunits that are differentially expressed between sexes in the targeting of polycomb.

120 Promoters in group B have medium to low levels of DNA methylation at E10.5 and are enriched for
121 H3K27me3 even before gonadal DNA demethylation. This group thus likely represents an
122 intermediate state. Similar to group A, group B has higher CpG density and higher GC content,
123 compared with group D ($P < 2 \times 10^{-16}$, pairwise Wilcoxon test), but higher GC enrichment than group A.
124 Interestingly, promoters in group A and B are enriched for germline-specific genes, such as *Stra8*,
125 *Sycp1*, *Sycp2*, *Dnmt3l* and *Tex101* (Extended Data Fig. 3a), whereas promoters in the group C
126 generally are linked to development and lineage-specific regulators (Extended Data Fig. 3a).

127 In order to functionally validate the importance of the observed dynamic changes in H3K27me3, we
128 depleted H3K27me3 in early PGCs using *Blimp1-Cre* (*Prdm1*) driven *Ezh2* deletion¹⁷. (Extended Data
129 Fig. 4b, 4c, 4d). EZH2 is highly expressed throughout the early germline development, compared
130 with surrounding somatic cells (Extended Data Fig. 4a). The expression of *Blimp1-Cre* begins at E7.0,
131 shortly after PGC specification, allowing us to deplete EZH2 before gonadal reprogramming occurs¹⁷.
132 Consistent with the reported high recombination efficiency of *Blimp1-Cre*¹⁸, EZH2 protein was absent
133 in gonadal *Ezh2*^{Δ/Δ}, *Blimp1-Cre* PGCs (Fig. 3a) (*Ezh2* conditional knock out is henceforth referred to
134 as *Ezh2* CKO). This coincided with the loss of H3K27me3 in *Ezh2* CKO PGCs, confirming that EZH2 is

135 the main enzyme responsible for catalysing H3K27me3 at this stage of PGC development (Fig. 3b,
136 Extended Data Fig. 6c). Of note, the loss of H3K27me3 did not affect global levels of H2A119ub or
137 H3K9me3, as evaluated by immunofluorescence (Extended Data Fig. 5a, 5b), or the global erasure of
138 DNA demethylation that occurs in gonadal PGCs (Extended Data Fig. 5c, 5d, 5e).

139 Although the observed loss of H3K27me3 did not have any apparent effect on the germ cell numbers
140 in both sexes at E13.5 (Extended Data Fig. 5f), RNA-Seq analysis showed clear separation by sex and
141 genotype (Ctrl vs CKO *Ezh2*^{-/-} PGCs) (Fig. 3c, Extended Data Fig. 6d). As anticipated based on our
142 H3K27me3 ChIP-Seq analysis (Fig. 1d), loss of EZH2 had a more profound impact on the
143 transcriptome of female PGCs (Fig. 3c, 3d) with 679 and 290 genes differentially expressed in female
144 and male *Ezh2*^{-/-} PGCs, respectively (adj. P<0.05 FC>2). Consistent with the role of PRC2 as a
145 transcriptional repressor, more than 80% of differentially expressed genes in male (239) and female
146 (565) were upregulated (Fig. 3d) with clear enrichment for cell differentiation, developmental
147 processes and gamete generation using Gene Ontology (GO) analysis (Fig. 3e, Extended Data Fig. 7a).
148 Importantly, loss of EZH2 affected specifically genes with promoters enriched in H3K27me3 in
149 control E13.5 PGCs (Extended Data Fig. 3a, 3b), documenting that following DNA demethylation,
150 promoter H3K27me3 is required for maintaining correct transcriptional regulation of these genes in
151 the developing germ line.

152 Amongst the genes upregulated in female E13.5 *Ezh2* CKO PGCs, we noticed an enrichment of genes
153 associated with reproduction and meiosis; out of 104 previously identified genes associated with
154 female meiotic prophase¹⁹, 31 genes were differentially expressed following *Ezh2* deletion (P=4X10⁻
155 ¹⁴) (Fig. 3f, Extended Data Fig. 7c). Similarly, depletion of EZH2 led to the transcriptional
156 derepression of 23 of the previously identified germline reprogramming-responsive (GRR) genes
157 (Extended Data Fig. 7g)⁹. H3K27me3 increased on the promoters of many meiosis-related genes
158 following the loss of DNA methylation between E10.5 to E13.5 (group A promoters), suggesting that
159 H3K27me3 deposition is required to modulate the expression of germline-specific, DNA methylation-
160 sensitive genes in the hypomethylated germ line (Extended Data Fig. 3a, 3b, Extended Data Fig 7d).

161 Although H3K27me3 enrichment on promoters of meiotic genes is observed in both male and
162 female PGCs (Fig. 3f, Extended Data Fig 7d), female PGCs show a much more profound
163 transcriptional response following EZH2 loss (Extended Data Fig. 7c). We reasoned that the presence
164 of signalling-induced, sex-specific transcription factors might be required to drive ectopic or
165 precocious transcription once the functional repressive chromatin mark is removed. To this end, the
166 presence of retinoic acid (RA) is essential for the transcriptional activation of *Stra8* and entry into
167 meiosis in the female germline. In contrast, RA is degraded in male gonads leading to diversion from

168 the meiotic programme²⁰. In agreement with our hypothesis, we found that RA-related transcription
169 factor binding motifs, such as RARB, RXRA and RARG are enriched in genes upregulated in female,
170 but not in male E13.5 *Ezh2* CKO PGCs. (Extended Data Fig. 7e). Furthermore, as expected, the
171 expression levels of these transcription factors are higher in the female germ cells than in the male
172 counterparts at E13.5 (Extended Data Fig. 7f). Taken together, RA signalling and the related
173 transcription factors present in the female germ line at this stage of development potentiate the
174 transcriptional response of the DNA hypomethylated genome upon removal of EZH2.

175 Although the loss of EZH2 led to precocious transcriptional upregulation of meiotic genes in female
176 *Ezh2* CKO PGCs, we did not observe any profound effect on the initial progression of the meiotic
177 prophase (Extended Data Fig. 6e, 8a, 8b). However, despite normal PGC number at E13.5, germ cell
178 numbers in *Ezh2*^{f/f}, *Blimp1-Cre* ovaries at E16.5 and E18.5 were significantly reduced (Fig. 3g). The
179 accumulation of γ H2A.X signal (Fig. 4a) specifically in female *Ezh2* CKO PGCs suggested the presence
180 of DNA damage, prompting us to examine the transcriptional regulation of transposable elements
181 (TEs) that when re-activated could compromise genome integrity. This revealed that many TE
182 subfamilies were upregulated predominantly in the E13.5 female *Ezh2* CKO PGCs (Fig. 4b), while only
183 very few differentially expressed TE subfamilies were identified in male *Ezh2* CKO PGCs (Extended
184 Data Fig. 9a). The same trend is observed when analysing uniquely mapped, single copy TEs (Fig. 4c,
185 Extended Data Fig. 9b). The derepression of TEs in female *Ezh2* CKO PGCs is further documented by
186 the upregulation of IAP-GAG and LINE1-ORF1 proteins (Fig. 4d) and the enrichment of P53 and
187 interferon-alpha response pathways in Gene Set Enrichment Analysis (GSEA) (Extended Data Fig. 9c,
188 9d). Both of these pathways have been previously linked to retrotransposon activation^{21,22}. In
189 addition, while most of RAD51 foci disappeared at E18.5, filament-like RAD51 signal was identified in
190 female *Ezh2* CKO germ cells, suggesting that unrepaired DNA damage persisted along the
191 chromosomes at this developmental stage (Extended Data Fig. 8b).

192 To understand the molecular underpinnings of the TE activation induced by EZH2 loss, we analysed
193 the repressive chromatin profile. This revealed that between E10.5 and E13.5 the levels of H3K9me3
194 increased on many evolutionarily young and potentially transcriptionally active LTR and non-LTR
195 retrotransposons, such as L1Md_A, IAP-d-int, and MMERVK10C, (Fig. 4e). In fact, more than 90% of
196 *de novo* H3K9me3 peaks identified in E13.5 PGCs are located within 1kb to TEs (Extended Data Fig.
197 9e), suggesting that H3K9me3 provides transcriptional repression of TEs in the absence of DNA
198 methylation. TEs tend to gain more H3K9me3 in the male germline, with newly identified peaks
199 often representing the spreading of a repressive domain (Fig. 4e, Extended Data Fig. 9f).

200 Interestingly, many H3K9me3-marked ERVK, ERV1 and LINE1 subfamilies, including L1Md_Gf, T, A,

201 IAP-d-int and RLTR10, also show an increase in H3K27me3 signal between E10.5 and E13.5 (Fig. 4e).
202 H3K9me3 and H3K27me3 do not usually overlap in somatic cells; however, the dynamic changes
203 observed in PGCs indicate that PRC2 is recruited to these TEs following global DNA demethylation
204 (after E10.5), suggesting a possible functional compensation for the DNA methylation loss. The TEs
205 solely enriched in H3K9me3 tend to be evolutionarily young, transcriptionally competent ERVs
206 (IAPEz.int, IAPLTR1.Mm), while the H3K27me3 enriched TEs tend to be TE relics that lost their
207 transcriptional potential (Charlie, Tigger elements) (Extended Data Fig. 10a). Further analysis at the
208 level of single uniquely mapped TEs revealed three types of histone modification enrichment:
209 H3K9me3 and H3K27me3 are enriched separately on different copies of TEs (Extended Data Fig. 10b);
210 with the copies showing pronounced 5mC loss attracting H3K27me3 while TEs associated with
211 higher levels of DNA methylation showing H3K9me3 enrichment (Extended Data Fig. 10b). However,
212 we also detected a surprising co-enrichment of H3K27me3 and H3K9me3 on some copies
213 particularly of LINE1 elements (Extended Data Fig. 10c) as previously suggested²³. Importantly, the
214 pattern of repressive histone modifications is specific to an individual integrated copy of TE rather
215 than being representative of the whole TE subfamily.

216

217 Soon following their entry into the developing genital ridge, mouse PGCs undergo a wave of global
218 DNA demethylation yielding the most hypomethylated state of genome ever observed during
219 development⁹. Surprisingly, however this loss of DNA methylation does not lead to widespread
220 transcriptional activation raising an important question regarding the regulation of transcriptional
221 programme and fidelity in the almost near absence of this major repressive epigenetic system⁹.
222 Using an ULI-nChIP approach, we have investigated the dynamics of alternative epigenetic silencing
223 marks H3K27me3 and H3K9me3 in the context of dynamic global DNA methylation changes
224 occurring in gonadal PGCs. Our results show that genome-wide DNA demethylation is accompanied
225 by global remodelling of both of these repressive histone modifications, resulting in a sex specific
226 heterochromatin signature observed in post-reprogramming E13.5 PGCs (Fig. 1d, 1e). Using a genetic
227 loss of function model, we further show that EZH2- mediated H3K27me3 is required to maintain
228 transcriptional repression in hypomethylated gonadal PGCs (Extended Data Fig. 3), reinstating that
229 PRC2 is necessary to prevent aberrant transcriptional activation when other stable silencing
230 mechanisms, such as DNA methylation, are absent. This is particularly apparent for germline
231 associated and developmental genes (Fig.3, Extended Data Fig. 3, Extended Data Fig. 10f); and
232 especially in the context of the developing early post reprogramming female germ line, where the
233 presence of RA signalling promotes entry into meiosis. Given that robust transcriptional activation

234 has been shown to override polycomb-mediated repression directly or indirectly^{24,25}, it is thus
235 plausible that the balance between promoter associated H3K27me3 and cell signalling induced
236 transcription factor repertoire regulates the correct timing of meiotic programme initiation in the
237 female germ line at this stage of development.

238 PRC1 has been previously reported to regulate meiosis-related gene expression in male and female
239 germ cells²⁶. Intriguingly, only a small number of previously identified PRC1 targets are dysregulated
240 in our *Ezh2* knockout system pointing to the non-redundant roles of PRC1 and PRC2 in the germ line
241 (Extended Data Fig. 10d).

242 Our study importantly reveals that next to silencing of coding genes, EZH2-mediated H3K27me3 is in
243 post reprogramming hypomethylated germ cells required to repress potentially active transposable
244 elements (Fig. 4, Extended Data Fig. 10f). Using a combination of WGBS and ULI-nChIP-Seq data, we
245 show that H3K27me3 is enriched on many TE subfamilies only after gonadal DNA demethylation (Fig.
246 4e) providing an alternative mode of transcriptional silencing. Loss of H3K27me3 results in profound
247 TE derepression, leading to DNA damage and eventually germ cell loss in the female germ line (Fig.
248 3g). Consistent with this, the elevation of TEs has been linked to foetal oocyte attrition²⁷. The
249 severity of the TE derepression in the female PGCs upon EZH2 loss is likely due to the sex specific
250 heterochromatin configuration observed in the developing germ line (Fig. 1d,e, 4e). Following the
251 gonadal 5mC loss, the global DNA methylation remains low for a long period of time during
252 oogenesis; whereas *de novo* DNA methylation ensues soon (from E15.5 onwards) in male germ cells
253²⁸. Additionally, the TE associated H3K9me3 enrichment is much more pronounced in male than in
254 female E13.5 PGCs (Fig. 4e), suggesting that the male germ line utilises H3K9me3 and DNA
255 methylation, in connection with SETDB1 and piRNA pathway^{29,30} to restrain TEs. In contrast,
256 H3K27me3 is indispensable for the repression of hypomethylated TEs in the female developing germ
257 cells. Our results thus show diversification of the epigenetic repressive systems in controlling the
258 integrated TEs (Extended Data Fig 10e) and explain the previously reported sex specific effect of the
259 *Setdb1* deletion (Liu et al.). Our observation is also conceptually consistent with the previous report
260 in cultured mouse ES cells indicating that H3K27me3 relocalise and silence certain groups of
261 retrotransposons upon rapid and extensive loss of DNA methylation³¹; although different groups of
262 TEs seem to be responsive to the H3K27me3 loss in our *in vivo* system (Extended Data Fig. 10e).
263 Intriguingly, the role of polycomb in controlling parasitic DNA is likely to be ancestral as documented
264 by the recent discovery of the role of the Enhancer-of-zeste like protein *Ez1* in the repression of
265 transposable elements in *Paramecium*³².

266 Collectively, our study reveals that PRC2-mediated H3K27me3 is dynamically remodelled and
267 provides a buffering system of transcriptional regulation to modulate the impact of DNA methylation
268 loss during development. We demonstrate that sequence characteristics of promoters play a critical
269 role in PRC2 recruitment following the removal of cytosine methylation with relatively subtle
270 differences in promoter base composition having a profound effect on H3K27me3 enrichment.
271 Although this has been suggested previously using the insertion of synthetic DNA fragments into
272 mESCs³³; our genome-wide analysis and genetic study *in vivo* provide to our knowledge the first
273 example of the functional interplay between DNA methylation and polycomb silencing systems in
274 the context of development. To this end, aberrant global DNA hypomethylation has been frequently
275 observed in cancer³⁴. As both EZH2 and DNA methyltransferases have been identified as therapeutic
276 targets³⁵, understanding of the crosstalk between epigenetic silencing systems is of a profound
277 importance to allow precise interpretation and prediction of the outcome of clinical interventions.

278 **Methods**

279 **Mice**

280 All animal experiments were carried out under the UK Home office Project License in the
281 Home Office designated facility.

282 For PGC isolation, Oct4-GFP mice (GOF 18ΔPE-EGFP)¹² were crossed with C57BL/6 mice. The
283 time of mating is determined by the appearance of vaginal plug at noon which is defined as
284 embryonic day 0.5 (E0.5). Germ line deletion of *Ezh2* in PGCs was achieved by crossing mice
285 containing loxP-flanked *Ezh2* allele, *Ezh2*^{f/f} mice³⁶ with *Blimp1 (Prdm1)-Cre* mice. Cre-
286 mediated recombination was detected in 55–76% of PGCs from E8.0¹⁷, 85% at E9.5 and
287 100% at E13.5¹⁸. To isolate ctrl and *Ezh2* CKO PGCs for RNA-seq experiments, *Ezh2*^{f/f} mice
288 were crossed with Oct4-GFP mice. For genotyping of embryos, embryo tails were digested in
289 genotyping buffer (50mM KCL, 10mM Tris HCL, 0.1mg/ml gelatin, 0.45% Tween 20 dissolved
290 in water) with 0.2 mg/ml Proteinase K (Qiagen) overnight at 55 °C. Proteinase K was
291 inactivated by incubating for 5 min at 95 °C. Genotyping PCR was carried out using REDTaq
292 ready mix (Sigma, R2523). The sex of the embryo from E12.5 onwards was determined by
293 the gross appearance of the gonad and confirmed by PCR. Primers for genotyping are in
294 (**Supplementary Table 5**).

295 **PGC isolation by flow cytometry**

296 The dissected genital ridges (from E11.5) or segments of embryos (E9.5-E10.5) were first
297 digested for 5 min at 37 °C using 0.05% Trypsin-EDTA (Gibco) or TrypLE Express (Gibco).
298 Enzymatic digestion was followed by neutralization with pre-warm DMEM (Gibco, 21969-
299 035), containing 10% foetal bovine serum (Gibco) and pipetting up and down 20-30 times,
300 followed by centrifugation 2,000 rpm for 3min to collect cells. Cells were subsequently

301 resuspended in DMEM/F-12 supplemented with hyaluronidase (300 µg/ml; Sigma) by
302 pipetting up and down 10-20 times to generate single cell suspensions. Following
303 centrifugation at 2,000 rpm for 3 min to collect cells, the cell pellet was resuspended in ice-
304 cold PBS supplemented with poly-vinyl alcohol (10 µg/ml, Sigma) and EGTA (0.4 mg/ml,
305 Sigma). GFP-positive cells were isolated using an Aria IIu (BD Bioscience) or Aria III (BD
306 Bioscience) flow cytometer.

307 **RNA-seq library preparation**

308 E13.5 PGCs from each embryo were sorted separately and centrifuged at 2,000 rpm for 3
309 min following liquid nitrogen snap freezing. Total RNA was extracted using ZR-Duet DNA and
310 RNA Mini Prep kit (Zymo). The genotype of embryos was determined by PCR. RNA quality
311 was measured by 2100 bioanalyzer (Agilent technologies). To prepare cDNA libraries, 1 ng
312 total RNA was used for cDNA synthesis amplification (11 cycles) using SMART-seq V4 Ultra
313 Low input RNA kit (Takara), according to the manufacturer's instructions. The cDNA was
314 sheared by Covaris S2 sonicator (peak: 175, Duty: 10, cycle: 200, duration: 240 secs)
315 (Covaris). Fragmented cDNA was indexed and converted to sequencing libraries using
316 NEBNext Ultra II DNA library Prep Kit (NEB) following the manufacturer's instructions. All
317 libraries were purified by AMPure XP beads (Beckman-Coulter) and sequenced on the
318 Illumina HiSeq 2500.

319 **Cryosection immunofluorescence staining**

320 The dissected embryonic trunk (E10.5) or genital ridges from embryos (E11.5-E18.5) were
321 fixed by 2% paraformaldehyde (PFA) for 30 min at 4 °C, washed 3x 10min in PBS and
322 incubated overnight in 30% sucrose in PBS at 4 °C. The samples were then mounted in O.C.T.
323 mounting medium (VWR) and stored at -80 °C. The mounted samples were sectioned for 10
324 µm using Leica cryostat (Leica CM1950). The cryosections were post-fixed with 2% PFA in
325 PBS for 3 min, washed 3x 5min in PBS and permeabilised with blocking buffer (1% bovine
326 serum albumin (BSA)/0.1% Triton in PBS). The primary antibodies were added in blocking
327 buffer and incubated with slides overnight at 4 °C. The slides were subsequently washed 3
328 times in blocking buffer and incubated with Alexa dyes conjugated secondary antibodies
329 (Molecular Probes) in blocking buffer for 1 hr at room temperature in the dark. Then the
330 slides were washed 2 times for 5 min in blocking buffer and one for 5 min in PBS. Finally, the
331 slides were treated with DAPI (0.1 µg/ml) for 20 min and mounted in Vectashield (Vector
332 Laboratories) and imaged by using a Leica SP5 confocal microscope.

333 For 5mC and 5hmC staining, post-fixed sections were first permeabilized for 30 min with
334 blocking buffer (1% BSA/0.5% Triton in PBS) and subsequently treated with RNase A (10
335 mg/ml, Roche) (in 1% BSA/PBS) for 1 hr at 37 °C. Followed by times for 5 min washes with
336 PBS, sections were incubated with pre-warmed 4N HCl for 10, 15 and 20 min at 37 °C to
337 denature genomic DNA, followed by three washes with PBS. After incubating for 30 min at
338 room temperature in 1% BSA/PBS containing 0.1% Triton X-100, the sections were

339 incubated with primary antibodies at 4 °C overnight in the same buffer. Sections were
340 subsequently washed three times in blocking buffer (1% BSA/0.1% Triton in PBS) for 5 min
341 and incubated with the corresponding combination of secondary antibodies in the same
342 buffer for 1 hr in the dark at room temperature. Secondary antibody incubation was
343 followed by three 5 min washes with PBS. DNA was then stained with propidium iodide (PI)
344 (0.5ug/ml). After a final wash in PBS for 10 min, the sections were mounted with Vectashield
345 (Vector Laboratories). Antibodies are listed in (**Supplementary Table 5**).

346 **Quantification and Image analysis**

347 All IF images were processed and merged by Image J FIJI. For quantification of IAP GAG and
348 LINE1 ORF1, the integrated intensity in cytoplasm was measured by Cell profiler 2.2.0. To
349 identify cytoplasm area, DAPI was used to mark the nucleus and MVH-positive cells were
350 selected. The measured integrated intensity values were normalised to the background of
351 each staining to obtain normalised integrated intensity. For γ H2AX, the intensity in the
352 nucleus was measured by Image J. The intensity in PGCs was divided by the intensity in the
353 somatic cells.

354 **Germ cell counting**

355 We counted MVH-positive germ cells in the every fifth cryosection throughout the entire
356 gonad. To calculate the total number of germ cells in each gonad, the numbers counted per
357 section were multiplied by 5. The calculated germ cell numbers in the E16.5 and E18.5 Ctrl
358 gonads are close to the previous report³⁷.

359 **Western blot for PGCs**

360 5000 Oct4-GFP positive PGCs and 5000 ES cells grown in serum-based medium were sorted
361 and centrifuged at 2,000 rpm for 3 min. Cells were lysed with 10ul RIPA buffer (Sigma,
362 RO278) with protease inhibitor cocktail (Roche Complete tables mini). Total lysate was
363 loaded into 12% acrylamide/bis gel and separated in running buffer (25 mM Tris base, 190
364 mM glycine, 0.1% sodium dodecyl sulfate (SDS)). The protein was transferred to a
365 nitrocellulose membrane (Amersham) after electrophoresis in transferring buffer (25 mM
366 Tris base, 190 mM glycine, 0.1% SDS, 20% methanol). The membrane was blocked by 5%
367 BSA in PBST (0.1% tween in PBS) for 30 min at room temperature. Primary antibodies were
368 added in PBST with 5% BSA and incubated with the membrane overnight at 4 °C (MVH:
369 1:1000, H3K27me3 and H3K9me3: 1:2000, H3: 1:5000). The membrane was washed 3 times
370 with PBST for 10 min. Horseradish peroxidase (HRP) conjugated secondary antibodies
371 (1:10000) incubated for 1 hr at room temperature and then wash 3 times with PBST.
372 Luminata Crescendo Western HRP substrate (WBLUR0100, Milipore) was used for detection
373 on Amersham imager 680. Antibodies are listed in (**Supplementary Table 5**).

374 **5mdC/5hmdC quantification by LC-MS/MS**

375 DNA was extracted from 1000-6000 PGCs using ZR-Duet DNA and RNA Mini Prep kit (Zymo)
376 and digested to nucleosides overnight at 37°C using a nucleoside digestion mix (NEB,
377 M0649). The nucleosides were separated on an Agilent RRHD Eclipse Plus C18 2.1 × 100 mm
378 1.8u column using the HPLC 1290 system (Agilent) and mobile phases 100% water 0.1%
379 formic acids and 80% methanol, 0.1% formic acids. Quantification was carried out in an
380 Agilent 6490 triple quadrupole mass spectrometer on multiple reaction monitoring mode
381 (MRM), by monitoring specific transition pair of m/z 250.1/134.1 for dC, 290.1/174.1 for dG,
382 264.1/148.1 for 5mdC and 280.1/164.1 for 5hmdC. To calculate the concentrations of
383 individual nucleosides, standard curves were generated (dC and dG from Berry and
384 Associated; 5mdC and 5hmdC from CarboSynth). All samples and standard curve points
385 were spiked with a similar amount of isotope-labelled synthetic nucleosides (13C15N-dC
386 and 13C15N-dG purchased from Silantes, and d3-mdC and d215N2-mhdC was obtained
387 from T. Carell, Center for Integrated Protein Science at the Department of Chemistry,
388 Ludwig-Maximilians-Universität München, Germany). The threshold for peak detection is a
389 signal-to-noise ratio (calculated with a peak-to-peak method) above 10. . Final
390 measurements were normalised by dividing by the dG level measured for the same sample.
391 Limit of detection (LOD) was 0.005 -250 fmol for 5mdC and 5hmdC, and 0.1-5000 for dC and
392 dG. Limit of quantification (LOQ) was 0.025 – 50 fmol for 5mdC and 5hmdC, and 1-1000 for
393 dC and dG.

394 **Ultra low-input native chromatin immunoprecipitation (ULI-nChIP)**

395 Ultra low-input nChIP-seq was performed as previously described^{10,11}. PGCs were FACS
396 sorted into cold PBS and were lysed by nuclei isolation buffer (Sigma, NUC-101). For E10.5,
397 PGCs were pooled from different embryos. 1000 PGCs were used for each ChIP reaction. For
398 E13.5, embryos from independent litters are used as biological replicates. Samples were
399 permeabilized with 0.1% Triton-X-100 /0.1% deoxycholate in PBS on ice. Samples were
400 digested with 200 U of micrococcal nuclease (NEB, M0247S) in digestion buffer at 21 °C for
401 7.5 mins and the reaction was stopped with 100 mM EDTA. An aliquot of chromatin (10%)
402 was used as an input control. Samples were pre-cleaned by protein A/G beads for 2 hrs at 4
403 °C. Meanwhile, 250 ng anti-H3K9me3 (Diagenode, C15410056) and anti-H3K27me3
404 (Millipore, 07-449) antibodies were incubated with protein A/G beads for 2 hrs at 4 °C.
405 Chromatin samples were incubated with antibody-bound beads overnight at 4 °C. Samples
406 were washed by two low-salt washes and one high salt wash and eventually DNA was eluted
407 from the beads for 1.5 hrs at 60 °C. For sizes selection, AMPure XP beads were used at 1.8:1
408 ratio. Library preparation was performed using a MicroPlex Library Preparation kit v2
409 (Diagenode, C05010013) following manufacturer's recommendations. Libraries were further
410 purified by AMPure XP beads at 1:1 ratio. Library quality was measured with a 2100
411 Bioanalyzer Instrument (Agilent) and library size was assessed with a Kapa library qPCR
412 quantification kit (Roche, KK4824). Library sequencing was performed in a 100bp paired-end
413 mode with a HiSeq 2500 System (Illumina) following manufacturer's recommendations.

414 **RNA-seq data analysis**

415 Published RNA-Seq datasets for E10.5, E12.5 male, E12.5 female, E14.5 male and E14.5
416 female PGCs⁹ were retrieved from Gene Expression Omnibus (GEO) under accession
417 GSE76958.

418 Paired-end 100bp sequencing reads were processed with trimmomatic (0.33)³⁸ for trimming
419 adapters and low quality reads, then aligned against Ensembl mouse genome (NCBIM37)
420 with Tophat2 (2.0.11)³⁹. Reference sequence assembly and transcript annotation were
421 obtained from Illumina iGenomes
422 (https://support.illumina.com/sequencing/sequencing_software/igenome.html). Gene-
423 based read counts were obtained using featureCounts function from Rsubread Bioconductor
424 package (1.24.2)^{40,41}. Normalisation was performed in DESeq2 Bioconductor package
425 (1.14.1)⁴² and data was rlog transformed to allow for visualisation by PCA and heat maps.
426 Differentially expressed gene (DEG) analysis was also performed with DESeq2 and DEGs
427 were defined with Benjamini-Hochberg adjusted P-value<0.05 and fold change > 2. Z score
428 for heat maps was calculated based on rlog transformed data⁴². Gene ontology analysis was
429 performed with goseq Bioconductor package (1.24)⁴³. After converting mouse gene symbol
430 to human gene symbol using the report of Human and Mouse Homology retrieved from
431 Mouse Genome Informatics (MGI, <http://www.informatics.jax.org>), Gene Set Enrichment
432 Analysis (GSEA 2.2.0)⁴⁴ was then performed with GseaPreranked tool using Hallmarks gene
433 set (h.all.v5.2.symbols.gmt). Motif analysis was performed with PWMEnrich Bioconductor
434 package (4.20.0). Sample distance matrix was calculated using Euclidean distance and then
435 hierarchical clustering was performed using the complete linkage method.

436 In order to compare our RNA-seq data with WT PGC RNA-seq data⁹ we used RUVseq
437 Bioconductor package (1.18.0)⁴⁵ to correct the batch effect with RUVg function and
438 argument k=1 before producing the PCA plot.

439 **ChIP-seq data analysis**

440

441 ChIP-seq and input libraries were sequenced and 100 bp paired-end reads were aligned to
442 UCSC mm9 mouse genome with BWA (0.7.5a)⁴⁶. Aligned reads were sorted by Picard
443 SortSam tool (1.9; Picard), and duplicated reads were removed by Picard MarkDuplicates
444 tool (1.9; Picard). Using samtools view (0.1.18) with arguments -F 4 -f 0x02, we only kept
445 properly paired reads for downstream analysis. Properly paired reads were also further
446 separated into uniquely mapped reads and multiple mapped reads (MAPQ=0) for repeat
447 sequence analysis. (Multiple mapped reads were randomly assigned to one of their mapped
448 genomic loci).

449

450 We created 2 kb bin windows along the mm9 genome and subsequently removed windows
451 overlap with mm9 blacklist regions^{47,48}. Read counts for each windows for ChIP and input
452 were obtained using featureCounts function from Rsubread. The ChIP signal was normalised
453 to input using DESeq2. Bins Per Million (BPM) was calculated same as TPM in RNAseq^{49,50}.

454

455 Peak calling was performed using MACS2 (2.1.0)⁵¹ with arguments -f BAMPE --broad -g mm.
456 To annotate the peaks to genomic regions, we used CHIPseeker in the Bioconductor package
457 (1.18.0)⁵² with default settings, i.e. if peak overlapped with multiple genomic features, the
458 annotation was assigned in the following priority: Promoter, 5' UTR, 3' UTR, Exon, Intron,
459 Downstream and Intergenic. Only L1, ERV1, ERVK and ERVL repetitive families were used to
460 calculate the distance between peaks and transposable elements.

461

462 **Transposable element analysis**

463

464 To annotate CHIP-seq and RNA-seq read counts to repetitive sequences, we used the
465 repeatmasker track without repeat classes 'Low_complexity' or 'Simple_repeat' from mm9
466 UCSC genome table browser.

467

468 For TE subfamily level (eg. L1Md_T, IAP-d-int...), both uniquely and multiple mapped reads
469 (multiple mapped reads were randomly assigned to one of their mapped genomic loci).
470 Differentially expressed transposable elements were identified using edgeR Bioconductor
471 package (3.26.5)⁵³. For single copy level, only uniquely mapped reads were considered.

472

473 **WGBS analysis**

474

475 Published WGBS datasets from wild type E10.5, E12.5 male and female PGCs⁹ were
476 retrieved from Gene Expression Omnibus (GEO) under accession GSE76971.
477 Low quality reads and adaptors were trimmed off using trim_galore (v0.4.4;
478 https://www.bioinformatics.babraham.ac.uk/projects/trim_galore/). Bismark⁵⁴ was then
479 applied with -bowtie2 -ambiguous -p 8 -multicore 4 -ambig_bam settings, and trimmed
480 reads were mapped to mm9 BS genome. Cytosine methylated and unmethylated coverage
481 reports were created by applying bismark_methylation_extractor. We focused on CpG sites
482 from the reports with at least 5 fold coverage, and methylation rate was calculated as count
483 methylated/(count methylated+count unmethylated).

484

485 **Promoter definition and classification**

486

487 Promoters were defined as -2000 bp to +500 bp relative TSS. For the heatmaps, we used 2
488 kb windows with at least 1 kb overlapped with defined promoters. Promoter-associated
489 transcripts were obtained from R Bioconductor package TxDb.
490 Mmusculus.UCSC.mm9.knownGene (v 3.2.2). We classified total 33158 promoters based on
491 the pattern of dynamic changes in DNA methylation and H3K27me3.

492 Group A: Loss of DNA methylation, Gain of H3K27me3 at E13.5.

493 *DNA methylation rate E10.5 > 0.2, DNA methylation rate E10.5 - E12.5 > 0,*

494 $\text{Log}_2((E13.5 \text{ H3K27me3})/(\text{ChIP input})) \geq 0$

$\text{Log}_2((E13.5 \text{ H3K27me3})/(\text{ChIP input})) - \text{Log}_2((E10.5 \text{ H3K27me3})/(\text{ChIP input})) \geq 0.5$

495 Group B: Median loss of DNA methylation, High H3K27me3 at both stages.

DNA methylation rate E10.5 > 0.1, DNA methylation rate E10.5 - E12.5 > 0

$\text{Log}_2((E13.5 \text{ H3K27me3})/(\text{ChIP input})) \geq 1$

$\text{Log}_2((E13.5 \text{ H3K27me3})/(\text{ChIP input})) - \text{Log}_2((E10.5 \text{ H3K27me3})/(\text{ChIP input})) < 0.5$

496 Group C: Low DNA methylation rate, High H3K27me3.

DNA methylation rate E10.5 < 0.1

$\text{Log}_2((E13.5 \text{ H3K27me3})/(\text{ChIP input})) \geq 1$

$\text{Log}_2((E13.5 \text{ H3K27me3})/(\text{ChIP input})) - \text{Log}_2((E10.5 \text{ H3K27me3})/(\text{ChIP input})) < 0.5$

497 Group D: Loss of DNA methylation, Low H3K27me3 at E13.5.
498 *DNA methylation rate E10.5 > 0.2, or DNA methylation rate E10.5 – E12.5 > 0*
499 *Log₂((E13.5 H3K27me3)/(ChIP input)) < 0.5*

500

501 Non-classified: the rest of promoters.

502

503 CpG obs/exp ratio, percentage of CpG dinucleotide and percentage of C or G were
504 calculated within 2kb window as previously reported⁵⁵.

505

506 **Statistical analysis**

507 All statistical analysis were performed using R or Graphpad software and are described in
508 the figure legends. Biological replicates for all experiments were based on embryos from
509 independent litters. Specifically, P values were calculated by Wilcoxon rank sum test
510 (Extended Data Fig. 2c, Fig. 3b, 7c). Adjusted P values were calculated by Wilcoxon rank sum
511 test and adjusted by Bonferroni correction (Fig. 2). P values were calculate by two-tailed
512 unpaired Student's t test (Fig.3g and Fig. 4a, 4d). Adjusted P values were calculated by
513 ANOVA and Tukey's post-hoc multiple comparison test (Extended Data Fig. 5e).

514 Box plots were plotted using Tukey's method. The upper and lower hinges represent the
515 first and the third quartiles. The central line represents the median. The upper end of the
516 whisker represents the lowest value among either the third quartile plus 1.5 X IQR or the
517 maximum value from the data set. The lower end of the whisker represents the largest
518 value among either the first quartile minus 1.5 X (IQR) or the minimum value from the data
519 set.

520 Box plots were generated by R package ggplot2 with argument outlier.shape = NA in (Fig. 2b
521 and extended data Fig.3b).

522 **Data availability**

523 ChIP-seq and RNA-seq data have been deposited in Gene Expression Omnibus (GEO) under
524 GSE141182.

525

526

527

528

529

530

531

530 **Figure Legends**

531 **Figure 1: Sex-specific remodelling of repressive histone modifications during genome-wide**
532 **DNA demethylation in PGCs.**

533 **a**, Overview of chromatin dynamics during mouse PGC development. *: The assessment is
534 based on immunofluorescence staining. **b**, Genomic distribution of H3K27me3 and
535 H3K9me3 peaks. **c**, Genome-wide correlation (Spearman's correlation coefficient, 2 kb bins,
536 whole genome) of H3K27me3 and H3K9me3 enrichment after normalised to the input. **d, e**,
537 Total H3K27me3 and H3K9me3 peak numbers at each PGC stage. Venn diagram showing
538 peaks overlapping between E10.5, E13.5 male and E13.5 female PGCs. Bar charts show
539 retained and *de novo* peaks. **f**, Western blot analysis of H3K27me3 (left) and H3K9me3 (right)
540 abundance based on 5000 mESCs and 5000 GFP-positive E13.5 PGCs. MVH: germ cell marker.
541 P value was calculated from 3 independent experiments by two-tailed Student's *t* test. Error
542 bar: standard deviation.

543 **Figure 2: Base composition determines H3K27me3 enrichment during gonadal DNA**
544 **demethylation.**

545 **a**, Heat map depicting the dynamics of DNA methylation and the enrichment of H3K27me3
546 at promoters. 4 groups of promoters were identified based on the dynamic patterns
547 between DNA methylation and H3K27me3 (See Methods). **b**, Sequence characteristics of
548 the promoters described in (Fig. 2a). adj. P values were calculated by pairwise comparison
549 using Wilcoxon rank sum test and adjusted by Bonferroni correction. ***: $P < 0.001$. **c**,
550 Dynamics of DNA methylation and H3K27me3 at all promoters with respect to their
551 sequence characteristics. Methylation rate and H3K27me3 enrichment are shown by the
552 colour gradient. Distribution of each dot's value is shown using rug plot along x axis and y
553 axis.

554

555 **Figure 3: Conditional *Ezh2* KO leads to wide-spread transcriptional derepression and loss**
556 **of germ cells in the female germ line.**

557 **a, b**, Immunofluorescence staining of EZH2 and H3K27me3 in gonadal sections ($n=2$). MVH:
558 germ cell marker. Yellow arrowheads indicate PGCs. DNA stained by DAPI (blue). Scale bar:
559 10 μ m. **c**, Principal component analysis (PCA) of RNA-seq data from E13.5 male and female
560 Ctrl and *Ezh2* CKO (*Ezh2*^{-/-}, *Blimp1-Cre*) PGCs at E13.5. **d**, Number of differentially expressed
561 (DE) genes using different fold change (FC) thresholds. adj. $P < 0.05$. **e**, Gene ontology (GO)
562 terms associated with DE genes (CKO vs Ctrl). **f**, Heat map of gene expression and chromatin
563 dynamics of promoters associated with meiotic prophase genes. P value was calculated
564 using Fisher exact test. **g**, Representative immunostaining of E18.5 Ctrl and *Ezh2* CKO female
565 gonad sections. DNA was stained by DAPI. Scale bar: 100 μ m. Dot plot shows the total

566 number of germ cells per ovary. Each dot represents one biological replicates. Error bars
567 indicate standard deviation. P values were calculated by two-tailed unpaired Student's t test.

568 **Figure 4 EZH2-mediated H3K27me3 regulates retrotransposon repression.**

569 **a**, Immunofluorescence staining for γ H2AX (biological replicates n=2). Quantification of the
570 staining per PGC nucleus shown on the right. Numbers indicate the numbers of analysed
571 PGC nuclei. DNA was stained by DAPI. Scale Bar: 10 μ m. **b**, Expression of TEs (Multiple
572 mapped plus uniquely mapped reads) in E13.5 PGCs (*Ezh2* CKO vs Ctrl). Significantly
573 upregulated TEs are labelled in red. (Fold change > 1, FDR < 0.1). **c**, Dot plot represents the
574 expression levels of individual TE copies. Each dot represents a single element in indicated
575 subfamilies. Only uniquely mapped reads were considered. **d**, Immunofluorescence staining
576 (top) and signal quantification (bottom) of IAP GAG and LINE1 ORF1 proteins. Biological
577 replicates n=2. Statistical analysis was carried out using two-tailed unpaired Student's t test.
578 **e**, Heat map showing H3K9me3 and H3K27me3 enrichment of TE subfamilies ranked by DNA
579 methylation levels at E10.5. Each row represents one TE subfamily. Both multiple mapped
580 and uniquely mapped reads were considered.

581 Extended data Figure 1

582 **Summary of ULI-nChIP-seq and genomic distribution of H3K27me3 and H3K9me3**
583 **enrichment.**

584 **a**, Experimental scheme of PGC isolation using Δ PE Oct4-GFP mice (GOF 18 Δ PE-GFP)¹².
585 ~1000 PGCs were used for ULI-nChIP-seq. **b**, Characteristics of the H3K27me3 and H3K9me3
586 ULI-nChIP-seq. Fraction of paired-end reads based on the mappability. Uniquely aligned
587 (dark green). Uniquely aligned duplicates (light green). Multiple aligned (blue). Unaligned
588 (grey). **c**, Scatter plot showing the correlation between 2 biological replicates using 2kb
589 window. Higher variability observed between E13.5 samples relates to slight difference in
590 developmental progression between different embryos and litters (embryos from
591 independent litters used as biological replicates). Pearson correlation coefficient is shown
592 on the top left. **d**, Genomic distribution of H3K27me3 and H3K9me3 peaks. More than 60%
593 of H3K27me3 peaks are associated with promoters or gene bodies. H3K9me3 peaks are
594 located mostly in distal intergenic regions and introns. **e**, Distribution of H3K27me3 and
595 H3K9me3 peaks relative to transcription start site (TSS). **f**, Bar chart showing proportion of
596 H3K27me3 and H3K9me3 peaks associated with TEs in the genome. **g**, Violin plot showing
597 the distribution of peak intensity in E10.5, E13.5 male and female PGCs. Peaks were
598 identified by MACS2 peak calling pipeline with broad peak setting (See Methods). **h**,
599 Distribution of H3K27me3 and H3K9me3 peak length. The number of short peaks increases
600 at E13.5 male PGCs, compared with peaks at E10.5.

601

602

603

604 Extended Data Figure 2

605 **Dynamics of DNA methylation and H3K27me3 at promoters during gonadal**
606 **reprogramming.**

607 **a**, Whole-genome bisulphite sequencing (WGBS) data from E10.5, E12.5 female and E12.5
608 male PGCs⁹. Density plot depicting DNA methylation levels at all promoters. **b**, Density plot
609 depicting H3K27me3 enrichment at all promoters. **c**, Violin plot of H3K27me3 levels at
610 promoters that lost DNA methylation (DNA methylation >0.2 at E10.5). **d**, Dynamics of DNA
611 methylation and H3K27me3 at all promoters. DNA methylation and H3K27me3 enrichment
612 are shown by colour gradient. Distribution of each dot's value is shown using rug plot along
613 x axis and y axis. **e**, Box plot shows H3K27me3 enrichment of low CpG density (CpG <4.1%)
614 promoters which gained H3K27me3 in the female PGCs following global loss of DNA
615 methylation. Box plots were presented by Tukey method. P values were calculated by
616 Wilcoxon rank sum test. ***: P <0.001.

617 Extended data Figure 3

618 **Dynamics of DNA methylation, H3K9me3 and H3K27me3 at promoters during gonadal**
619 **reprogramming.**

620 **a**, Heat map depicting the H3K27me3 and H3K9me3 enrichment (ULI-nChIP-seq), and DNA
621 methylation rate (WGBS) at promoters. The promoters were grouped based on the pattern
622 of dynamic change between DNA methylation and H3K27me3 (See also Fig. 2). Group A: loss
623 of DNA methylation, gain H3K27me3 at E13.5. Group B: median loss of DNA methylation,
624 high H3K27me3. Group C: low DNA methylation, High H3K27me3. Group D: loss of DNA
625 methylation, low H3K27me3 at E13.5. Promoters that did not meet the criteria were
626 grouped into non-classified. The expression levels of promoter-associated genes from RNA-
627 seq are presented by TPM (Transcripts Per Kilobase Million) or z-score. The total number of
628 promoters in each group are shown on the left. **b**, Box plot showing the quantitative
629 measurement in each category, female and male PGCs, respectively. P values were
630 calculated by Wilcoxon rank sum test. **c**, Venn diagram showing the number of overlapped
631 promoters between male and female PGCs.

632 Extended Data Figure 4

633 **Generation of the germline specific *Ezh2* conditional knock out.**

634 **a**, Representative immunofluorescence (IF) staining for EZH2 using cryosectioned genital
635 ridges. EZH2 is highly expressed during PGC development, compared with surrounding
636 somatic cells. Biological replicates n=3. OCT4: PGC marker. DAPI indicates DNA. Scale bar:
637 10um. **b**, Functional domains of EZH2 protein and targeting strategy of *Ezh2* allele. Open
638 boxes: exons. Black arrowhead: loxP sites **c**, Breeding scheme for germline *Ezh2* knockout.
639 *Ezh2*^{Δ/Δ}, Tg (*Blimp1-Cre*) refers to CKO in the figures. f: allele flanked by loxP sites (floxed).

640 Δ : Deleted allele generated using Cre-mediated recombination. Tg (*Blimp1-Cre*): transgenic
641 mice express Cre recombinase under the control of *Blimp1* (*Prdm1*) promoter. **d**, Deleted
642 alleles were confirmed by genotyping using the primers shown by black arrows in (**b**). #1:
643 *Ezh2*^{f/ Δ} , Tg (*Blimp1-Cre*)+/- . #2: *Ezh2*^{f/+}

644 Extended Data Figure 5

645 **Global H3K9me3, H2A119ub and DNA methylation are not altered in PGCs following the**
646 **loss of EZH2.**

647 **a, b, c**, Representative IF staining for H3K9me3, H2A119ub and TET1 using cryosectioned
648 genital ridges. MVH: PGC marker. Biological replicates n=2. **d**, IF staining for 5-
649 methylcytosine (5mC). 5mC is enriched in pericentromeric regions in the nucleus of somatic
650 cells but depleted in both Ctrl and *Ezh2* CKO germ cells. **e**, Global 5mC and 5hmC levels were
651 measured by LC-MS/MS. Each dot represents one biological replicate. Mean values of
652 5mdC/dG or 5hmdC/dG are shown. adj. P values were calculated using ANOVA and Tukey's
653 post-hoc multiple comparison test. **f**, Representative IF images of E13.5 Ctrl and *Ezh2* CKO
654 female and male gonads. DNA was stained by DAPI. Scale bar: 100 μ m. The bar chart shows
655 the total number of germ cells per female gonad. Error bars indicate standard deviation.
656 Biological replicates n=2.

657 Extended data Figure 6

658 **Transcriptome analysis of Ctrl and *Ezh2* CKO PGCs.**

659 **a**, Catalytic core and accessory subunits of mammalian PRC2. **b**, RNA expression of PRC2
660 components during germ cell development. **c**, RNA expression of *Ezh1* in the Ctrl and *Ezh2*
661 CKO germ cells. **d**, Sample distance matrix of RNA-seq samples by non-supervising cluster
662 (see Methods). **e**, PCA Plot shows the distance of transcriptomes from different PGC
663 developmental stages. Dash line circle indicates samples of the same developmental stage.

664 Extended Data Figure 7

665 **Sex-specific transcription factor repertoire determines transcriptional activation upon loss**
666 **of EZH2.**

667 **a**, Gene ontology (GO) terms associated with E13.5 $\text{\textcircled{M}}$ DE genes (Ctrl vs CKO). **b**, Integrative
668 Genomics Viewer (IGV) plot shows the H3K27me3 enrichment and RNA-seq read counts of
669 *Strat8*. Mouse genome: mm9. **c**, Heat map depicting gene expression and the chromatin
670 dynamics at promoters of meiotic differentially expressed (DE) genes. Box plot shows the
671 H3K27me3 enrichment and RNA expression (TPM) of meiotic DE genes in male and female
672 PGCs. Z scores were calculated for male and female separately. P values were calculated by
673 Wilcoxon rank sum test. ***: P<0.01 **d**, Bar chart showing the odds ratio of 104 meiosis
674 prophase genes¹⁹ in each groups of promoters (Fig. 2). P values were calculated by Fisher
675 exact test. *: P<0.05. **: P<0.01. ***: P<0.001. **e**, Promoters of upregulated genes in female

676 *Ezh2* CKO are significantly enriched for transcription factor motifs that relate to retinoid acid
677 signalling pathway. Motif analysis was performed using Bioconductor package PWMEnrich. **f**,
678 Heat map shows the relative gene expression of identified transcription factors in male and
679 female PGC samples. **g**, Heat map shows gene expression of 45 Germline Reprogramming
680 Responsive (GRR) genes in Ctrl and *Ezh2* CKO samples. Differentially expressed genes are
681 shown on the top (adj. P<0.05).

682 Extended Data 8

683 **Loss of *Ezh2* does not lead to precocious meiotic prophase**

684 **a**, Representative IF images of the meiotic specific synaptonemal complex protein SCP3 in
685 embryonic ovaries. Axial element alignment was observed in female E18.5 germ cells. **b**,
686 Representative IF images of cryosectioned gonads. γ H2AX signal shows DNA double strand
687 breaks (DSBs) occurring during homologous recombination. Accumulation of γ H2AX signal in
688 E16.5 ctrl and *Ezh2* CKO germ cells, this is greatly reduced at E18.5. A number RAD51 foci
689 can be identified at E16.5 but greatly decreases at E18.5. Filament-like, RAD51-positive
690 structure was identified in the *Ezh2* CKO germ cells but not in Ctrl germ cells. Germ cells are
691 indicated by yellow arrowhead and are positive for MVH. DAPI indicates DNA. Scale bar:
692 10um.

693 Extended Data Figure 9

694 **EZH2-mediated H3K27me3 regulates TE repression.**

695 **a**, Differential expression analysis of TE expression in E13.5 male PGCs (CKO vs Ctrl).
696 Significantly upregulated TEs are labelled in red. Fold change > 1, FDR< 0.1. **b**,
697 Multidimensional scaling (MDS) plot showing distance of Ctrl and *Ezh2* CKO samples based
698 on TE expression. Only uniquely mapped reads were considered. **c**, Gene Set Enrichment
699 Analysis (GSEA) of DE genes(E13.5♀ CKO vs Ctrl). Number of genes enriched in each gene
700 set is shown by the circle size. **d**, GSEA plot showing genes upregulated in female *Ezh2* CKO
701 PGCs are enriched in p53 pathway and interferon alpha response. FDR q value < 0.25 was
702 considered significant. NES: normalized enrichment score. **e**, Analysis of distance between
703 H3K9me3 *de novo* peaks, transcription start sites (TSS) and transposable elements (TEs).**f**,
704 Representative IGV plot showing H3K9me3 enrichment on IAP Ez elements.

705 Extended Data Figure 10

706 **H3K9me3 enrichment on TEs and co-localisation with H3K27me3.**

707 **a**, TE subfamilies enriched predominantly for H3K9me3 or H3K27me3. Each row represents
708 one TE subfamily. Multiple mapped and uniquely mapped reads were taken into account. **b**,
709 **c**, Heat map showing DNA methylation, H3K9me3 and H3K27me3 enrichment at individual
710 copies of IAPLTR2_Mm and L1Md_Gf. Each row represents one uniquely mapped, single TE
711 copy belonging to the respective TE subfamily. **d**, Venn diagram depicting overlap of genes

712 upregulated in the *Ezh2* CKO female PGCs and the *Rnf2* CKO PGCs²⁶. **e**, Venn diagram
713 showing overlap between the EZH2 and SETDB1 regulated TEs in mouse germ cells and
714 between the EZH2 regulated TEs in germ cells and the EED regulated TEs in mESCs^{23,31}. **f**,
715 Model depicting the relationship between DNA demethylation and heterochromatin
716 changes in gonadal PGCs undergoing epigenetic reprogramming.

717

718

719 **Acknowledgements**

720 We thank J. Elliot, T. Adejumo and B. Patel for help with the fluorescence activated cell sorting, C.
721 Whilding for the help with microscopy and IF data analysis, L. Game for the help with next-
722 generation sequencing, Z. Agate-Bacon and G. Zimmerman for mouse husbandry, T. Carell (LMU
723 Munich) for providing isotopically labelled deoxynucleoside standards and the members of the
724 Hajkova laboratory for discussions and revisions of the manuscript. Work in the Hajkova laboratory is
725 supported by MRC funding (MC_US_A652_5PY70) and an ERC grant (ERC-CoG-648879–
726 dynamicmodifications) to P.H. P.H. acknowledges membership in the EMBO Young Investigator
727 Programme. T.C.H. is a recipient of Imperial College London/Taiwan Top University Strategic Alliance
728 PhD Scholarship.

729

730 **Author Contributions**

731 T.C.H and P.H. conceived the study; T.C.H performed the experiments and analysed the data; Y.F.W.
732 analysed the next-generation sequencing data; E.V-F. carried out the ULI-nChIP with the help of C.H.
733 and G.K.; C.E.R. carried out LC–MS/MS; T.C.H. and P.H. wrote the manuscript.

734

735

736

- 737 1 Robertson, K. D. DNA methylation and human disease. *Nat Rev Genet* **6**, 597-610,
738 doi:10.1038/nrg1655 (2005).
- 739 2 Guibert, S., Forne, T. & Weber, M. Global profiling of DNA methylation erasure in mouse
740 primordial germ cells. *Genome research* **22**, 633-641, doi:10.1101/gr.130997.111 (2012).
- 741 3 Hackett, J. A. *et al.* Germline DNA demethylation dynamics and imprint erasure through 5-
742 hydroxymethylcytosine. *Science* **339**, 448-452 (2013).
- 743 4 Seisenberger, S. *et al.* The Dynamics of Genome-wide DNA Methylation Reprogramming in
744 Mouse Primordial Germ Cells. *Molecular Cell* **48**, 849-862 (2012).
- 745 5 Seki, Y. *et al.* Cellular dynamics associated with the genome-wide epigenetic reprogramming
746 in migrating primordial germ cells in mice. *Development* **134**, 2627-2638,
747 doi:10.1242/dev.005611 (2007).
- 748 6 Hajkova, P. *et al.* Chromatin dynamics during epigenetic reprogramming in the mouse germ
749 line. *Nature* **452**, 877-881, doi:nature06714 [pii]

750 10.1038/nature06714 (2008).

751 7 Hajkova, P. Epigenetic reprogramming in the germline: towards the ground state of the
752 epigenome. *Philos Trans R Soc Lond B Biol Sci* **366**, 2266-2273, doi:10.1098/rstb.2011.0042
753 (2011).

754 8 Spiller, C., Koopman, P. & Bowles, J. Sex Determination in the Mammalian Germline. *Annu*
755 *Rev Genet* **51**, 265-285, doi:10.1146/annurev-genet-120215-035449 (2017).

756 9 Hill, P. W. S. *et al.* Epigenetic reprogramming enables the transition from primordial germ
757 cell to gonocyte. *Nature* **555**, 392-396, doi:10.1038/nature25964 (2018).

758 10 Brind'Amour, J. *et al.* An ultra-low-input native ChIP-seq protocol for genome-wide profiling
759 of rare cell populations. *Nat Commun* **6**, 6033, doi:10.1038/ncomms7033 (2015).

760 11 Hanna, C. W. *et al.* MLL2 conveys transcription-independent H3K4 trimethylation in oocytes.
761 *Nature structural & molecular biology* **25**, 73-82, doi:10.1038/s41594-017-0013-5 (2018).

762 12 Yoshimizu, T. *et al.* Germline-specific expression of the Oct-4/green fluorescent protein (GFP)
763 transgene in mice. *Dev Growth Differ* **41**, 675-684 (1999).

764 13 Juan, A. H. *et al.* Roles of H3K27me2 and H3K27me3 Examined during Fate Specification of
765 Embryonic Stem Cells. *Cell Rep* **18**, 297, doi:10.1016/j.celrep.2016.12.036 (2017).

766 14 Li, H. *et al.* Polycomb-like proteins link the PRC2 complex to CpG islands. *Nature* **549**, 287-
767 291, doi:10.1038/nature23881 (2017).

768 15 Wang, X. *et al.* Molecular analysis of PRC2 recruitment to DNA in chromatin and its inhibition
769 by RNA. *Nature structural & molecular biology* **24**, 1028-1038, doi:10.1038/nsmb.3487
770 (2017).

771 16 Mendenhall, E. M. *et al.* GC-rich sequence elements recruit PRC2 in mammalian ES cells.
772 *PLoS genetics* **6**, 1-10 (2010).

773 17 Ohinata, Y. *et al.* Blimp1 is a critical determinant of the germ cell lineage in mice. *Nature* **436**,
774 207-213, doi:10.1038/nature03813 (2005).

775 18 Li, Z. *et al.* The Sm protein methyltransferase PRMT5 is not required for primordial germ cell
776 specification in mice. *EMBO J* **34**, 748-758, doi:10.15252/embj.201489319 (2015).

777 19 Soh, Y. Q. *et al.* A Gene Regulatory Program for Meiotic Prophase in the Fetal Ovary. *PLoS*
778 *genetics* **11**, e1005531, doi:10.1371/journal.pgen.1005531 (2015).

779 20 Bowles, J. & Koopman, P. Retinoic acid, meiosis and germ cell fate in mammals.
780 *Development* **134**, 3401-3411, doi:10.1242/dev.001107 (2007).

781 21 De Cecco, M. *et al.* L1 drives IFN in senescent cells and promotes age-associated
782 inflammation. *Nature* **566**, 73-78, doi:10.1038/s41586-018-0784-9 (2019).

783 22 Jackson-Grusby, L. *et al.* Loss of genomic methylation causes p53-dependent apoptosis and
784 epigenetic deregulation. *Nat Genet* **27**, 31-39, doi:10.1038/83730 (2001).

785 23 Liu, S. *et al.* Setdb1 is required for germline development and silencing of H3K9me3-marked
786 endogenous retroviruses in primordial germ cells. *Genes and Development* **28**, 2041-2055,
787 doi:10.1101/gad.244848.114 (2014).

788 24 Riising, E. M. *et al.* Gene silencing triggers polycomb repressive complex 2 recruitment to
789 CpG islands genome wide. *Mol Cell* **55**, 347-360, doi:10.1016/j.molcel.2014.06.005 (2014).

790 25 Schmitges, F. W. *et al.* Histone methylation by PRC2 is inhibited by active chromatin marks.
791 *Mol Cell* **42**, 330-341, doi:10.1016/j.molcel.2011.03.025 (2011).

792 26 Yokobayashi, S. *et al.* PRC1 coordinates timing of sexual differentiation of female primordial
793 germ cells. *Nature* **495**, 236-240, doi:10.1038/nature11918 (2013).

794 27 Malki, S., van der Heijden, G. W., O'Donnell, K. A., Martin, S. L. & Bortvin, A. A role for
795 retrotransposon LINE-1 in fetal oocyte attrition in mice. *Dev Cell* **29**, 521-533,
796 doi:10.1016/j.devcel.2014.04.027 (2014).

797 28 Saitou, M., Kagiwada, S. & Kurimoto, K. Epigenetic reprogramming in mouse pre-
798 implantation development and primordial germ cells. *Development* **139**, 15-31, doi:10.1093/dev/139/1/15
799 [pii]

800 10.1242/dev.050849 (2012).

801 29 Pezic, D., Manakov, S. A., Sachidanandam, R. & Aravin, A. A. piRNA pathway targets active
802 LINE1 elements to establish the repressive H3K9me3 mark in germ cells. *Genes and*
803 *Development* **28**, 1410-1428, doi:10.1101/gad.240895.114 (2014).

804 30 Inoue, K., Ichiyangi, K., Fukuda, K., Glinka, M. & Sasaki, H. Switching of dominant
805 retrotransposon silencing strategies from posttranscriptional to transcriptional mechanisms
806 during male germ-cell development in mice. *PLoS genetics* **13**, e1006926,
807 doi:10.1371/journal.pgen.1006926 (2017).

808 31 Walter, M., Teissandier, A., Perez-Palacios, R. & Bourc'his, D. An epigenetic switch ensures
809 transposon repression upon dynamic loss of DNA methylation in embryonic stem cells. *Elife*
810 **5**, doi:10.7554/eLife.11418 (2016).

811 32 Frapporti, A. *et al.* The Polycomb protein Ezh1 mediates H3K9 and H3K27 methylation to
812 repress transposable elements in Paramecium. *Nat Commun* **10**, 2710, doi:10.1038/s41467-
813 019-10648-5 (2019).

814 33 Wachter, E. *et al.* Synthetic CpG islands reveal DNA sequence determinants of chromatin
815 structure. *Elife* **3**, e03397, doi:10.7554/eLife.03397 (2014).

816 34 Ehrlich, M. DNA hypomethylation in cancer cells. *Epigenomics* **1**, 239-259,
817 doi:10.2217/epi.09.33 (2009).

818 35 Jones, P. A., Issa, J. P. & Baylin, S. Targeting the cancer epigenome for therapy. *Nat Rev*
819 *Genet* **17**, 630-641, doi:10.1038/nrg.2016.93 (2016).

820 36 Su, I. H. *et al.* Ezh2 controls B cell development through histone H3 methylation and Igh
821 rearrangement. *Nature immunology* **4**, 124-131, doi:10.1038/ni876 (2003).

822 37 Malki, S., Tharp, M. E. & Bortvin, A. A Whole-Mount Approach for Accurate Quantitative and
823 Spatial Assessment of Fetal Oocyte Dynamics in Mice. *Biology of reproduction* **93**, 113,
824 doi:10.1095/biolreprod.115.132118 (2015).

825 38 Bolger, A. M., Lohse, M. & Usadel, B. Trimmomatic: a flexible trimmer for Illumina sequence
826 data. *Bioinformatics* **30**, 2114-2120, doi:10.1093/bioinformatics/btu170 (2014).

827 39 Kim, D. *et al.* TopHat2: accurate alignment of transcriptomes in the presence of insertions,
828 deletions and gene fusions. *Genome Biol* **14**, R36, doi:10.1186/gb-2013-14-4-r36 (2013).

829 40 Liao, Y., Smyth, G. K. & Shi, W. The Subread aligner: fast, accurate and scalable read mapping
830 by seed-and-vote. *Nucleic Acids Res* **41**, e108, doi:10.1093/nar/gkt214 (2013).

831 41 Liao, Y., Smyth, G. K. & Shi, W. featureCounts: an efficient general purpose program for
832 assigning sequence reads to genomic features. *Bioinformatics* **30**, 923-930,
833 doi:10.1093/bioinformatics/btt656 (2014).

834 42 Love, M. I., Huber, W. & Anders, S. Moderated estimation of fold change and dispersion for
835 RNA-seq data with DESeq2. *Genome Biol* **15**, 550, doi:10.1186/s13059-014-0550-8 (2014).

836 43 Young, M. D., Wakefield, M. J., Smyth, G. K. & Oshlack, A. Gene ontology analysis for RNA-
837 seq: accounting for selection bias. *Genome Biol* **11**, R14, doi:10.1186/gb-2010-11-2-r14
838 (2010).

839 44 Subramanian, A. *et al.* Gene set enrichment analysis: a knowledge-based approach for
840 interpreting genome-wide expression profiles. *Proc Natl Acad Sci U S A* **102**, 15545-15550,
841 doi:10.1073/pnas.0506580102 (2005).

842 45 Risso, D., Ngai, J., Speed, T. P. & Dudoit, S. Normalization of RNA-seq data using factor
843 analysis of control genes or samples. *Nat Biotechnol* **32**, 896-902, doi:10.1038/nbt.2931
844 (2014).

845 46 Li, H. & Durbin, R. Fast and accurate short read alignment with Burrows-Wheeler transform.
846 *Bioinformatics* **25**, 1754-1760, doi:10.1093/bioinformatics/btp324 (2009).

847 47 Consortium, E. P. An integrated encyclopedia of DNA elements in the human genome.
848 *Nature* **489**, 57-74, doi:10.1038/nature11247 (2012).

849 48 Amemiya, H. M., Kundaje, A. & Boyle, A. P. The ENCODE Blacklist: Identification of
850 Problematic Regions of the Genome. *Sci Rep* **9**, 9354, doi:10.1038/s41598-019-45839-z
851 (2019).

852 49 Ramirez, F. *et al.* deepTools2: a next generation web server for deep-sequencing data
853 analysis. *Nucleic Acids Res* **44**, W160-165, doi:10.1093/nar/gkw257 (2016).

854 50 Li, B. & Dewey, C. N. RSEM: accurate transcript quantification from RNA-Seq data with or
855 without a reference genome. *BMC Bioinformatics* **12**, 323, doi:10.1186/1471-2105-12-323
856 (2011).

857 51 Zhang, Y. *et al.* Model-based analysis of ChIP-Seq (MACS). *Genome Biol* **9**, R137,
858 doi:10.1186/gb-2008-9-9-r137 (2008).

859 52 Yu, G., Wang, L. G. & He, Q. Y. CHIPseeker: an R/Bioconductor package for ChIP peak
860 annotation, comparison and visualization. *Bioinformatics* **31**, 2382-2383,
861 doi:10.1093/bioinformatics/btv145 (2015).

862 53 Robinson, M. D., McCarthy, D. J. & Smyth, G. K. edgeR: a Bioconductor package for
863 differential expression analysis of digital gene expression data. *Bioinformatics* **26**, 139-140,
864 doi:10.1093/bioinformatics/btp616 (2010).

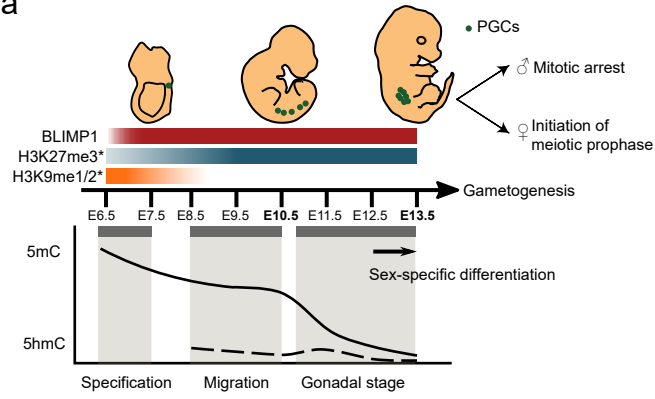
865 54 Krueger, F. & Andrews, S. R. Bismark: a flexible aligner and methylation caller for Bisulfite-
866 Seq applications. *Bioinformatics* **27**, 1571-1572, doi:10.1093/bioinformatics/btr167 (2011).

867 55 Gardiner-Garden, M. & Frommer, M. CpG islands in vertebrate genomes. *J Mol Biol* **196**,
868 261-282, doi:10.1016/0022-2836(87)90689-9 (1987).

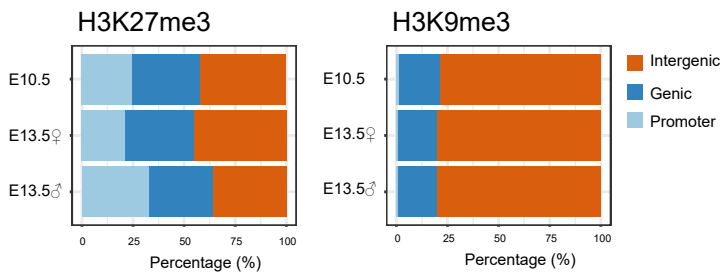
869

Figure 1

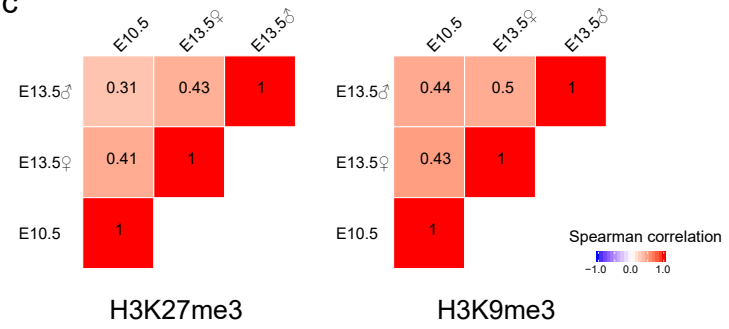
a



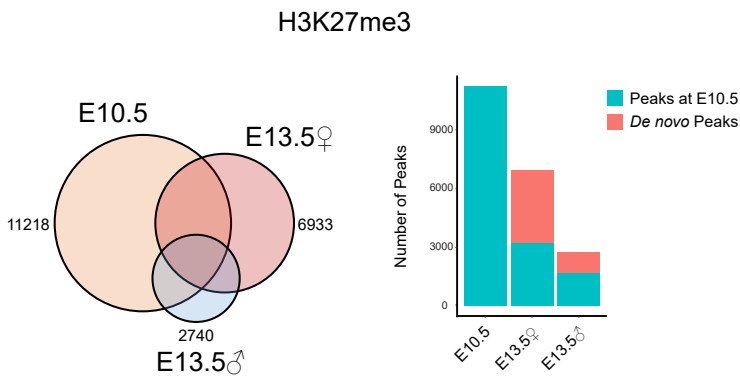
b



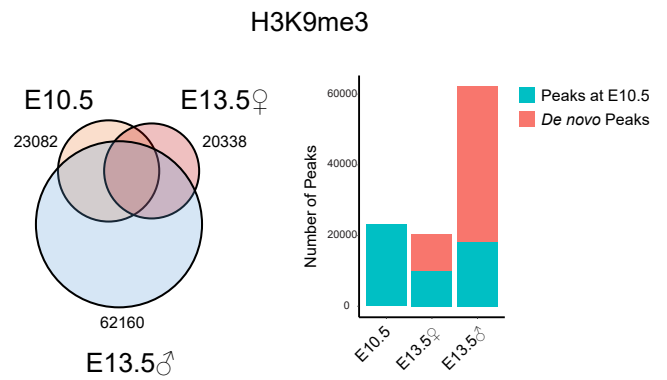
c



d



e



f

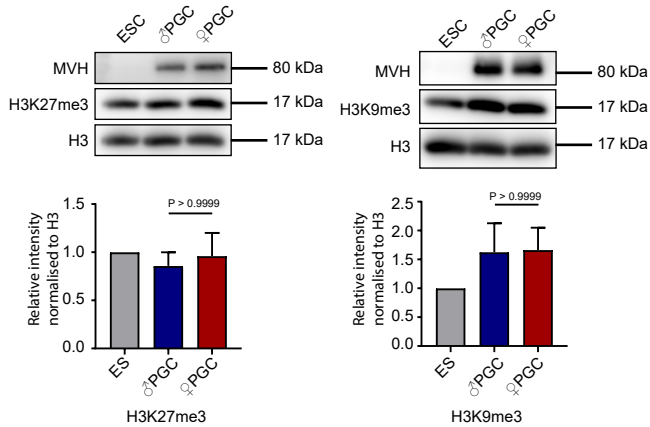


Figure 2

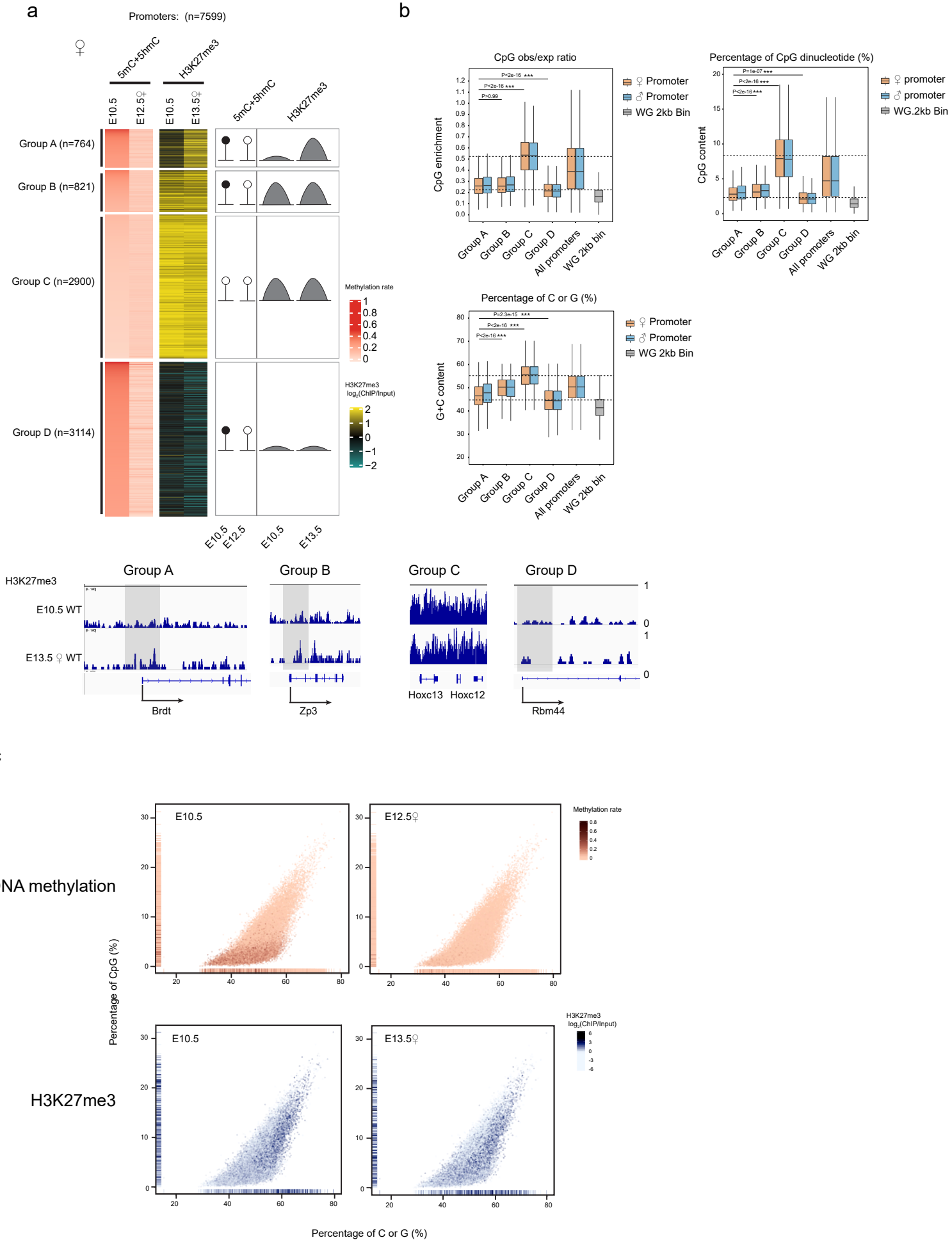
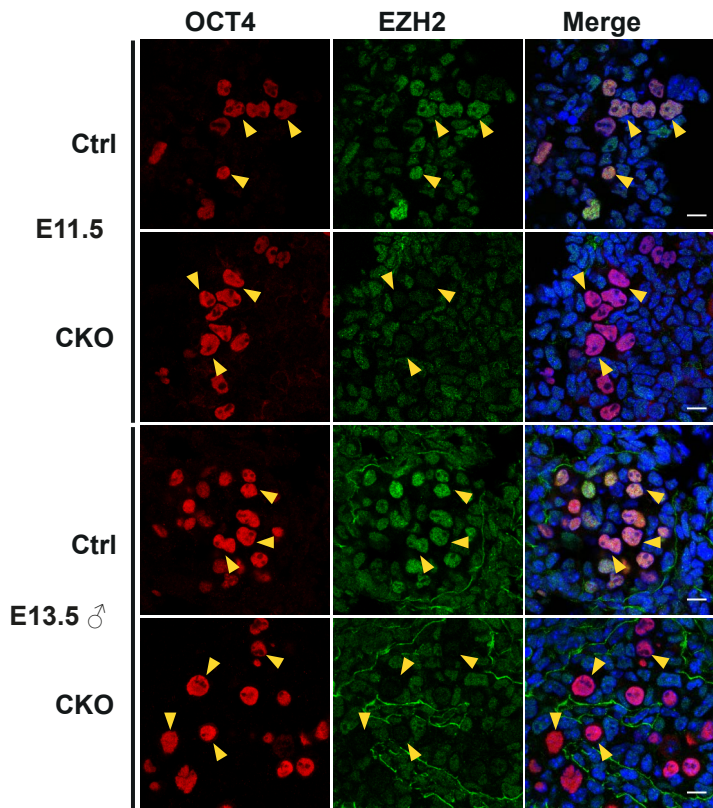
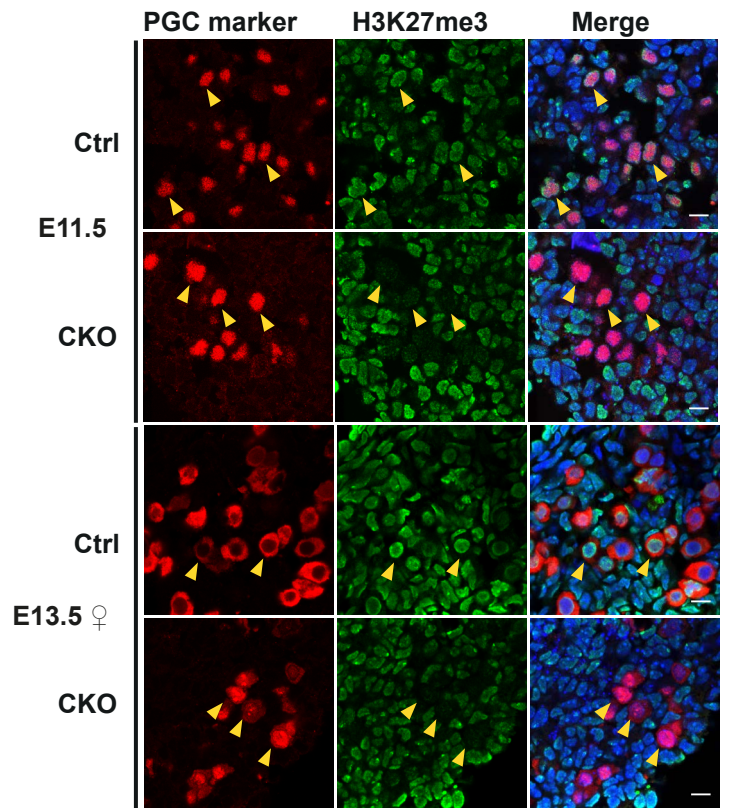


Figure 3

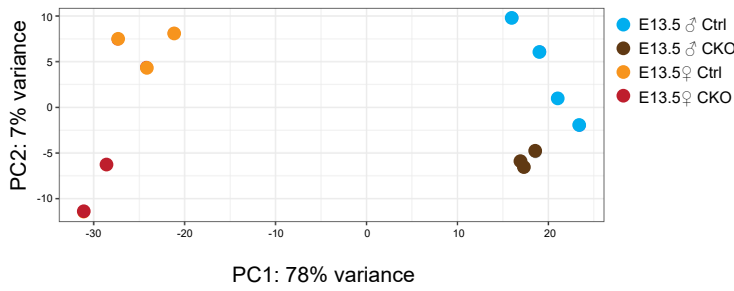
a



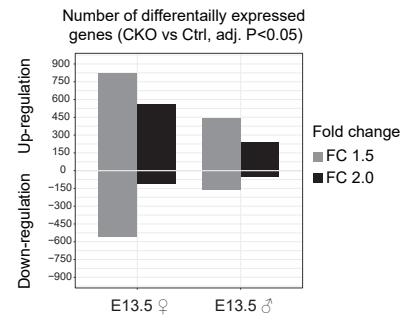
b



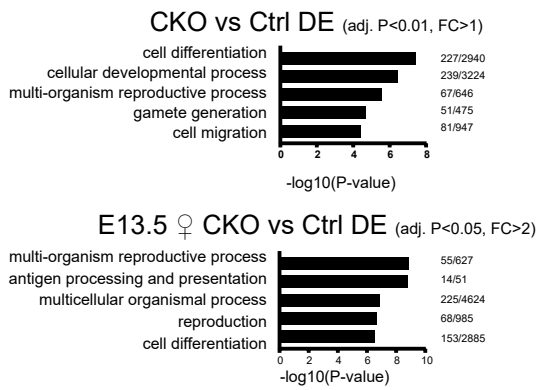
c



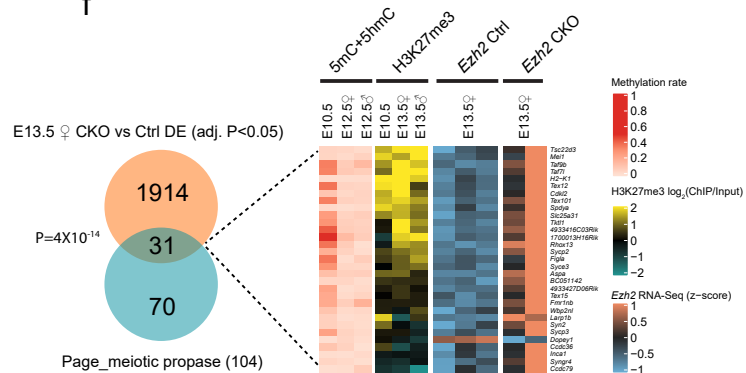
d



e



f



g

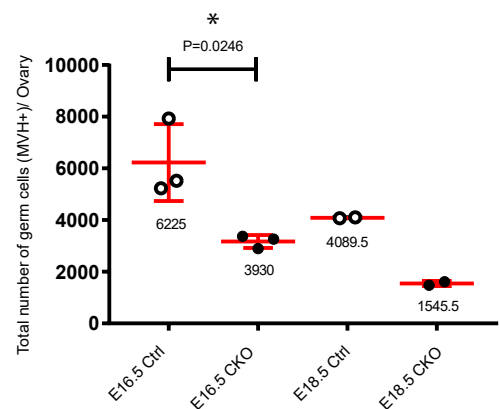
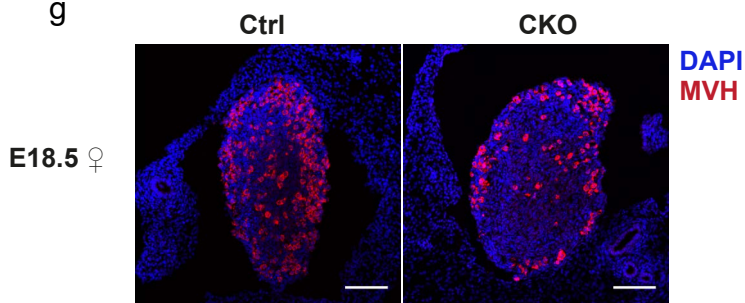
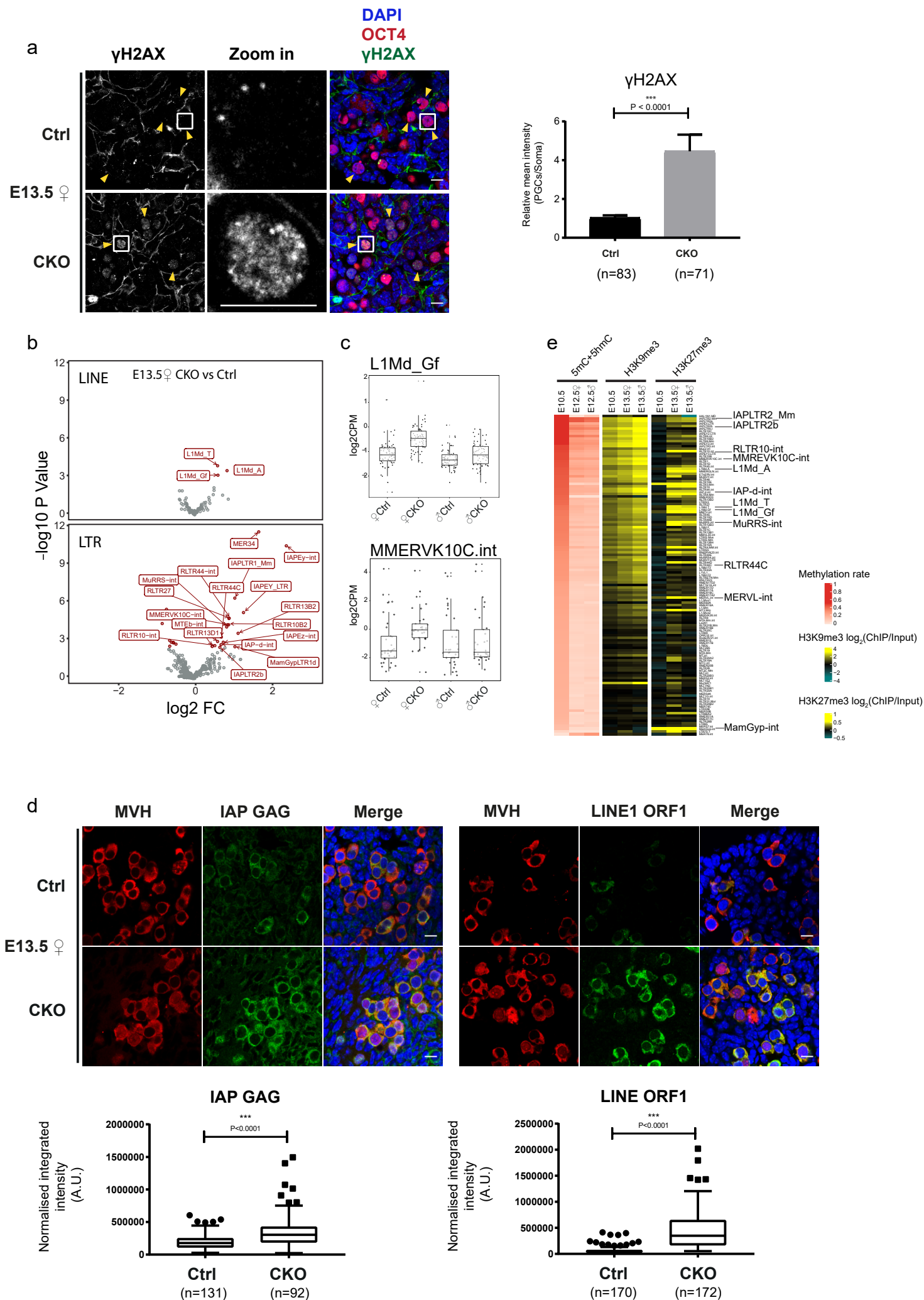
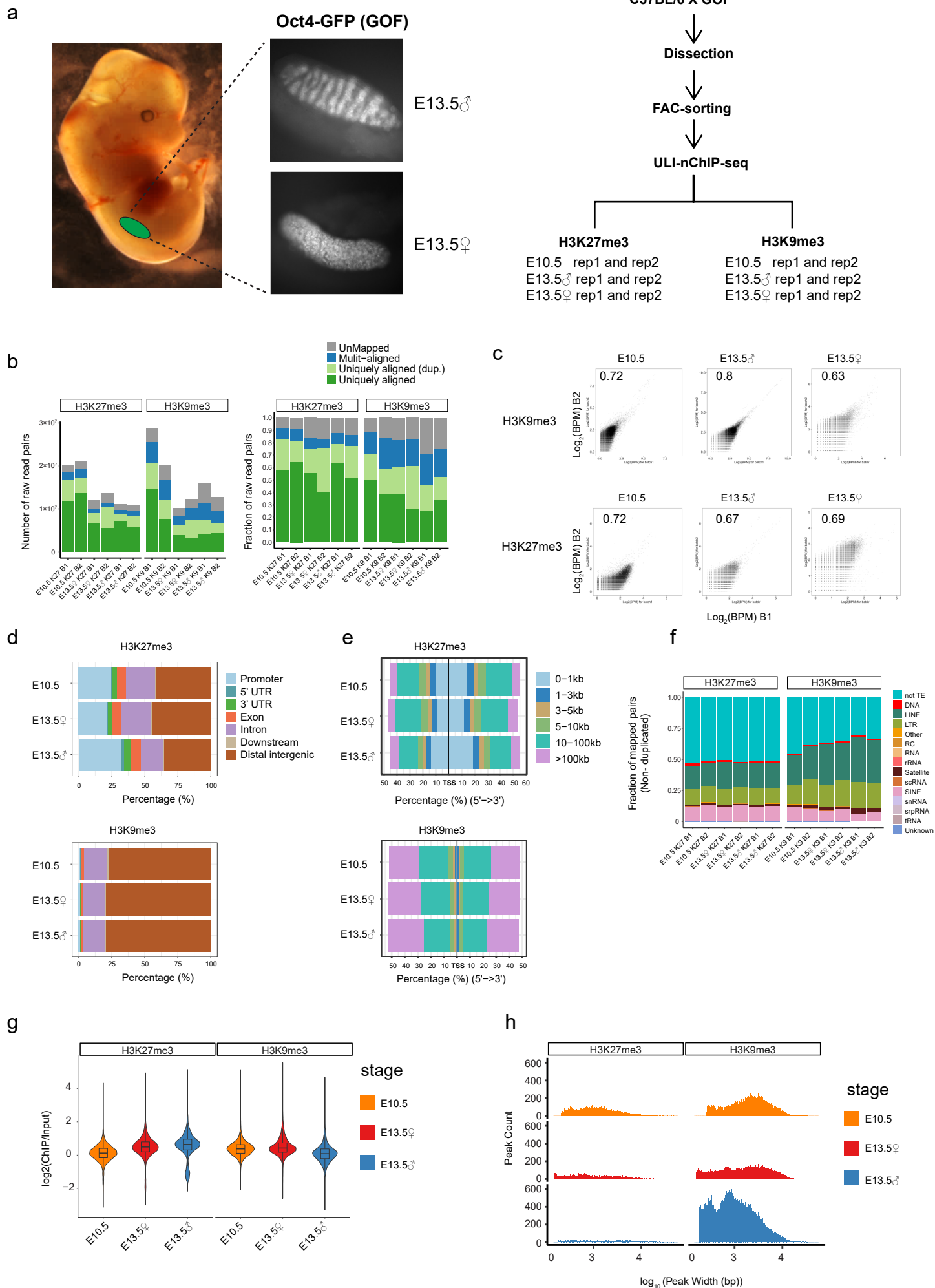


Figure 4

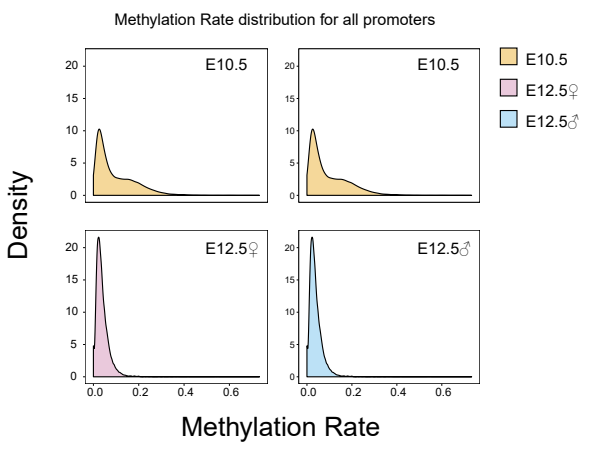


Extended Data Figure 1

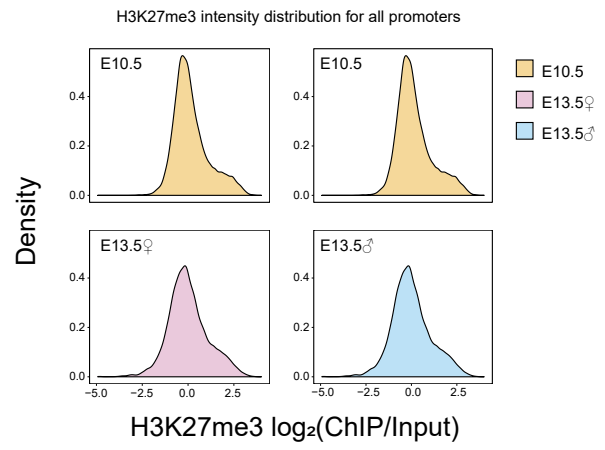


Extended Data Figure 2

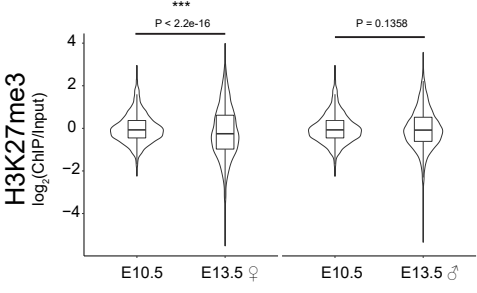
a



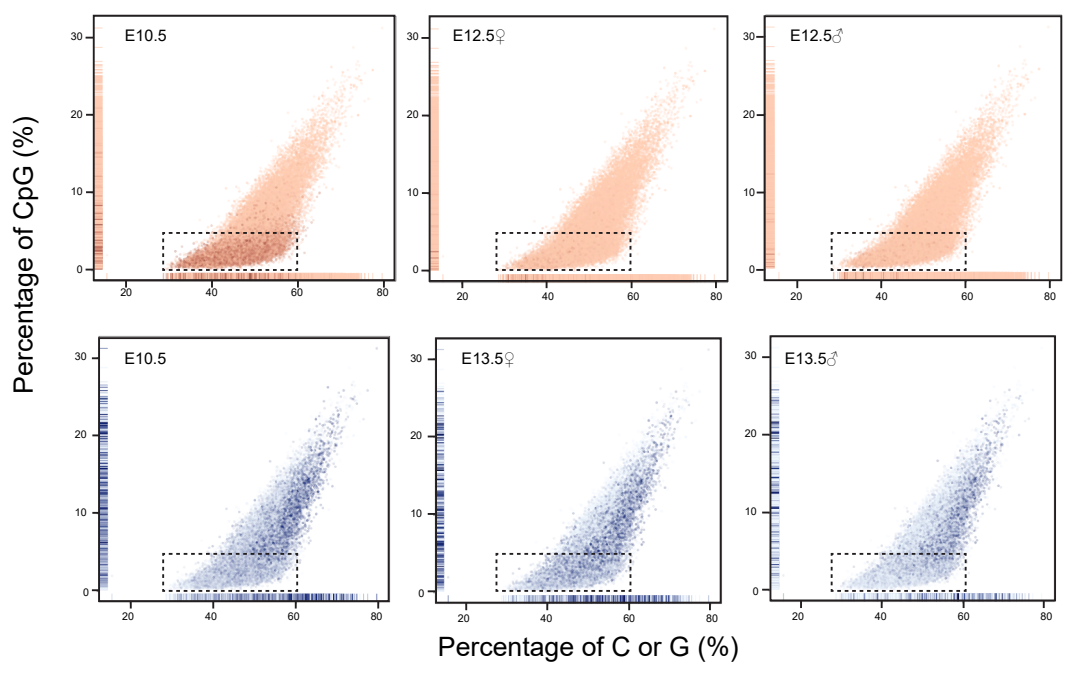
b



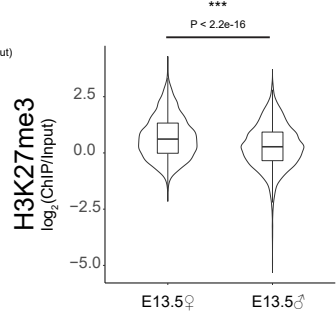
c



d



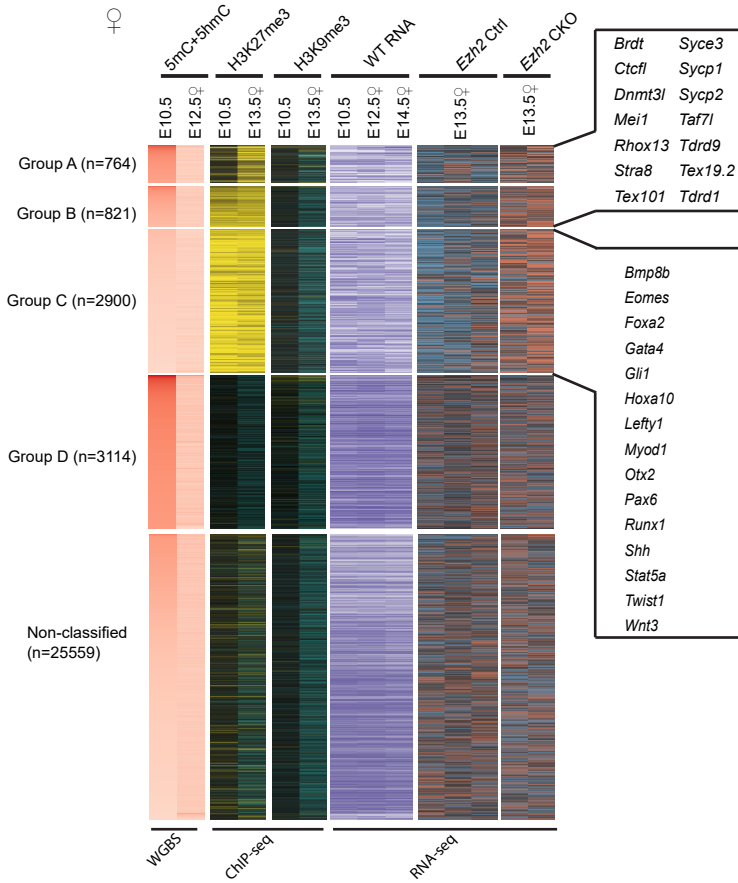
e



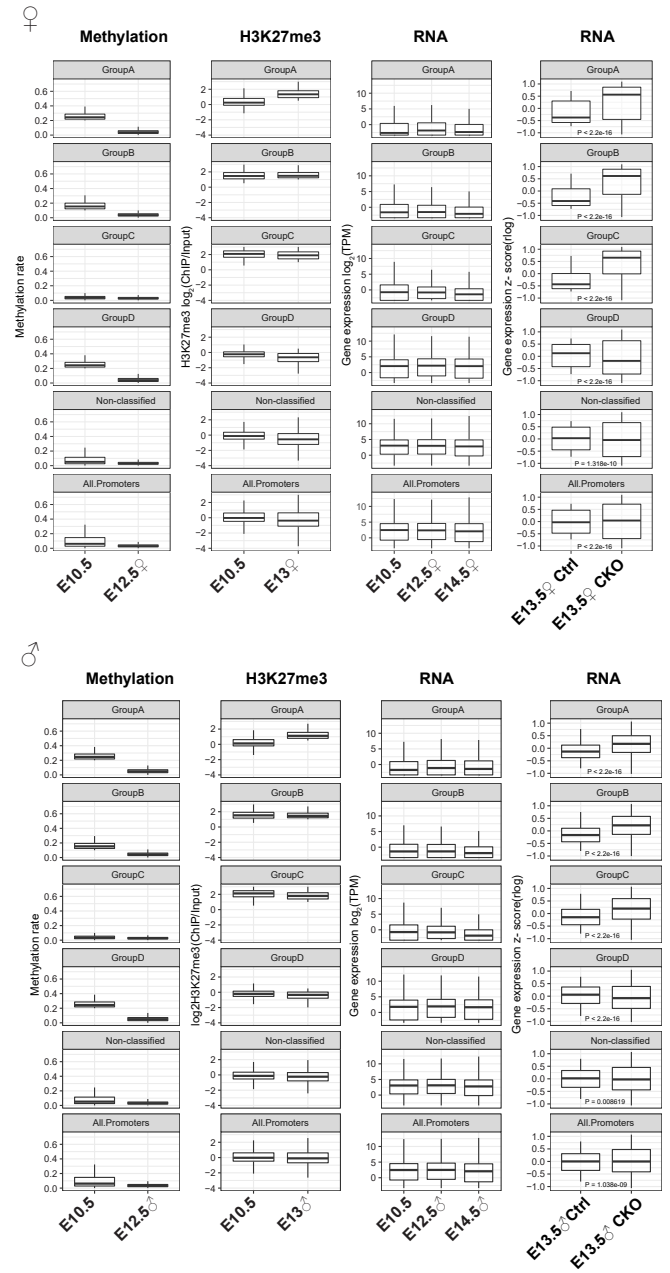
Extended Data Figure 3

a

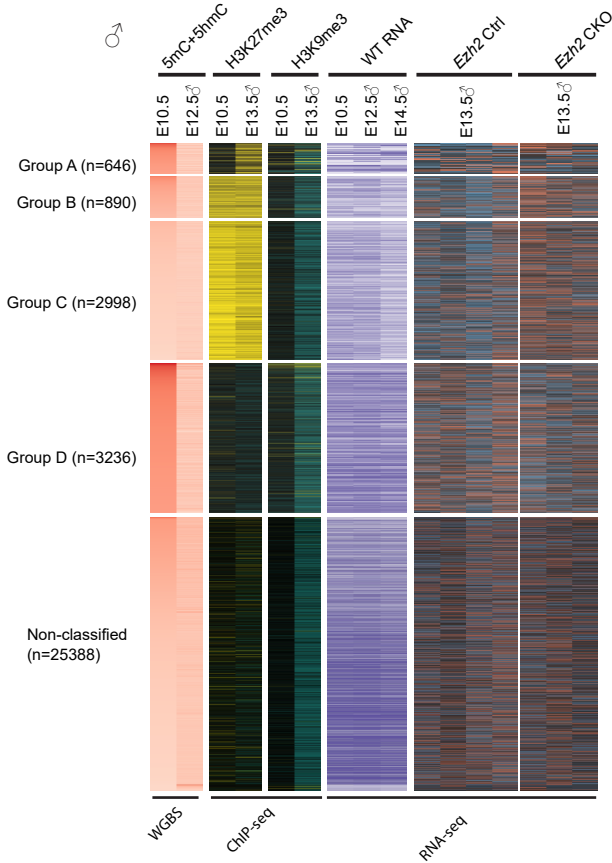
Promoter Regions: (n=33158)



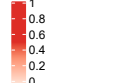
b



Promoter Regions: (n=33158)



Methylation rate



H3K27me3 $\log_2(\text{ChIP/Input})$



H3K9me3 $\log_2(\text{ChIP/Input})$



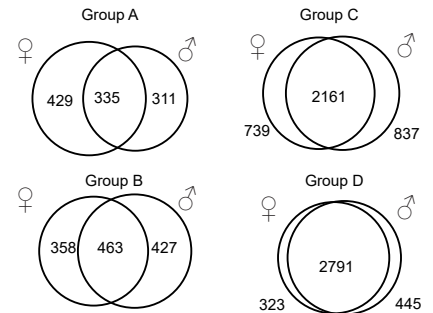
WT RNAseq (TPM)



Ezh2 RNA-Seq (Z-score)

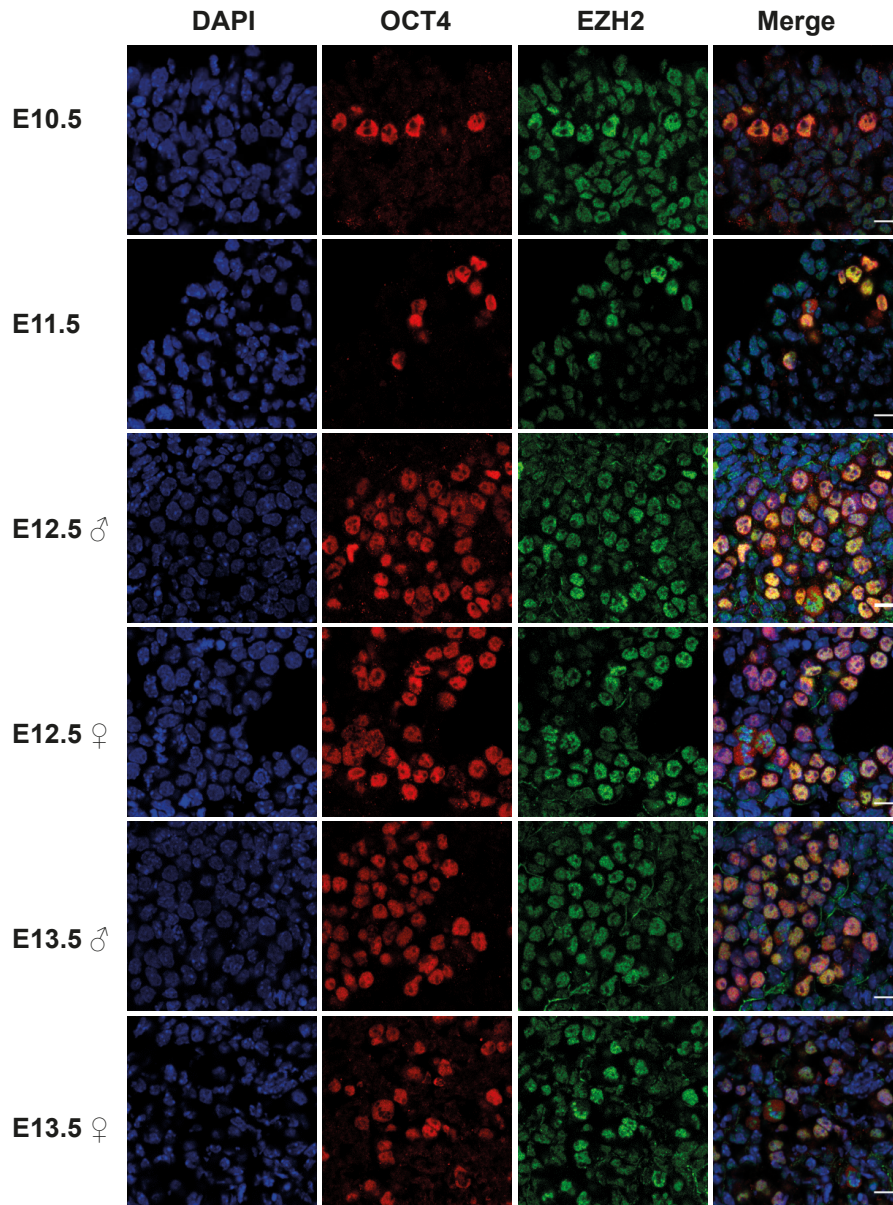


c

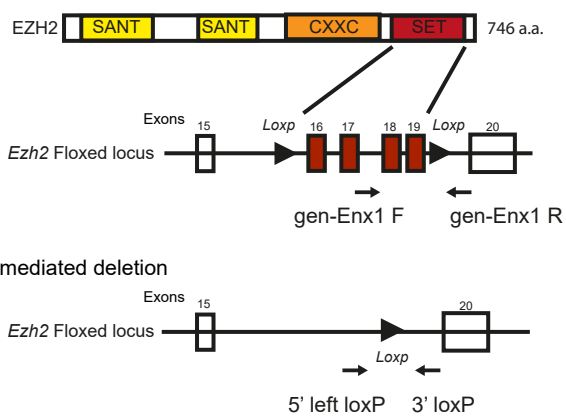


Extended Data Figure 4

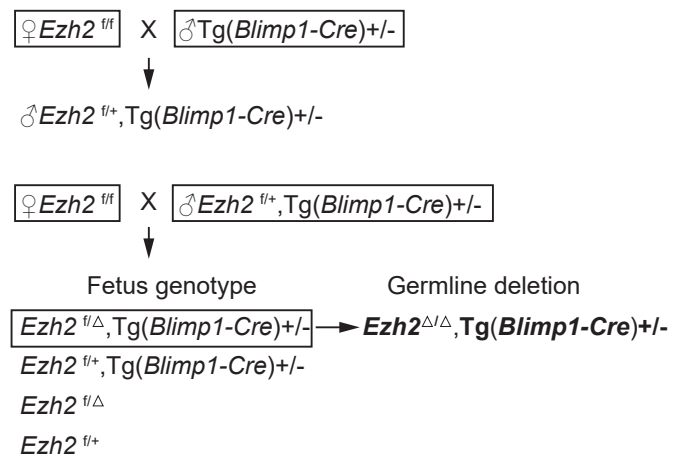
a



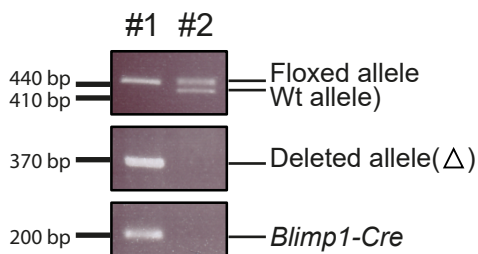
b



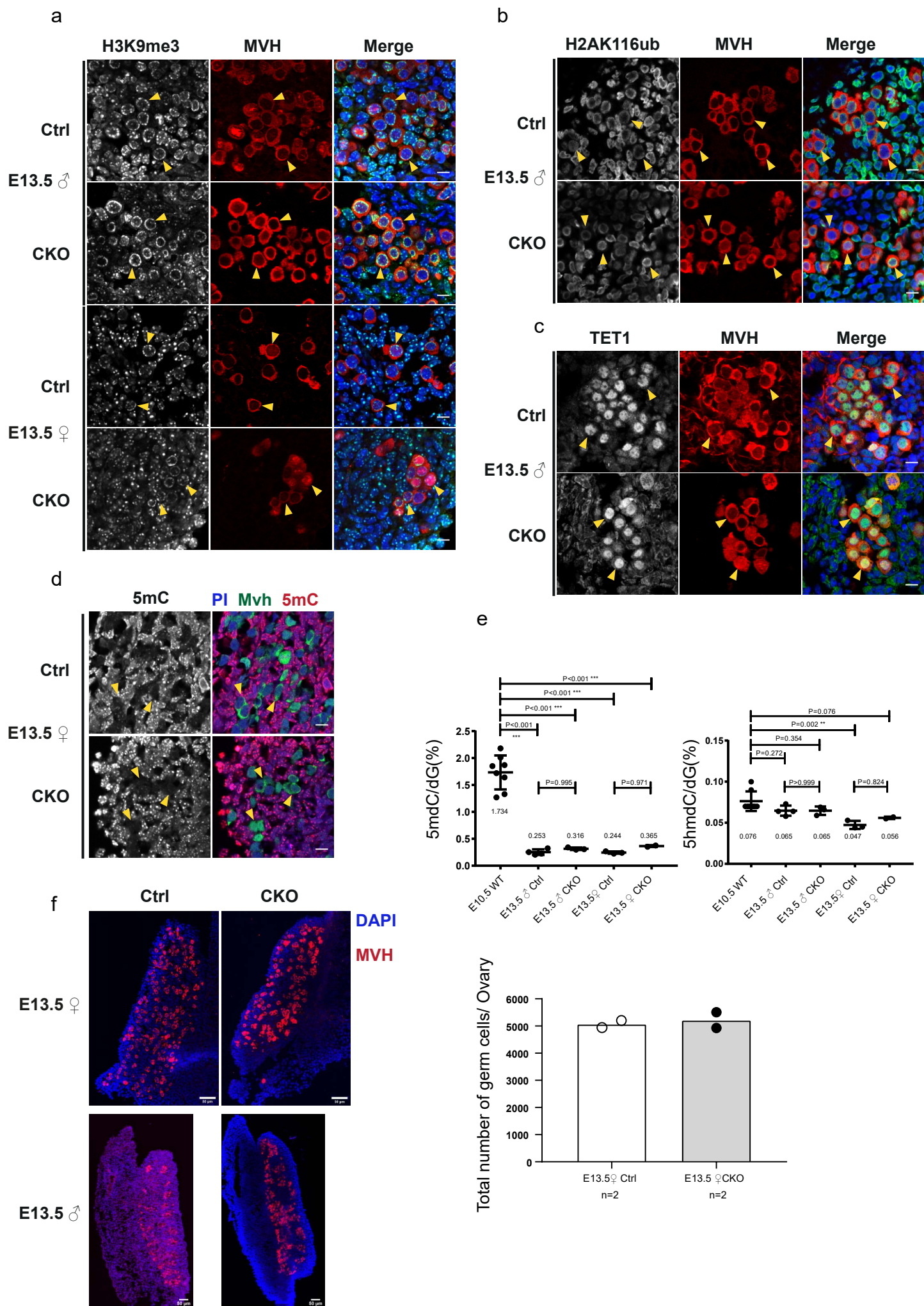
c



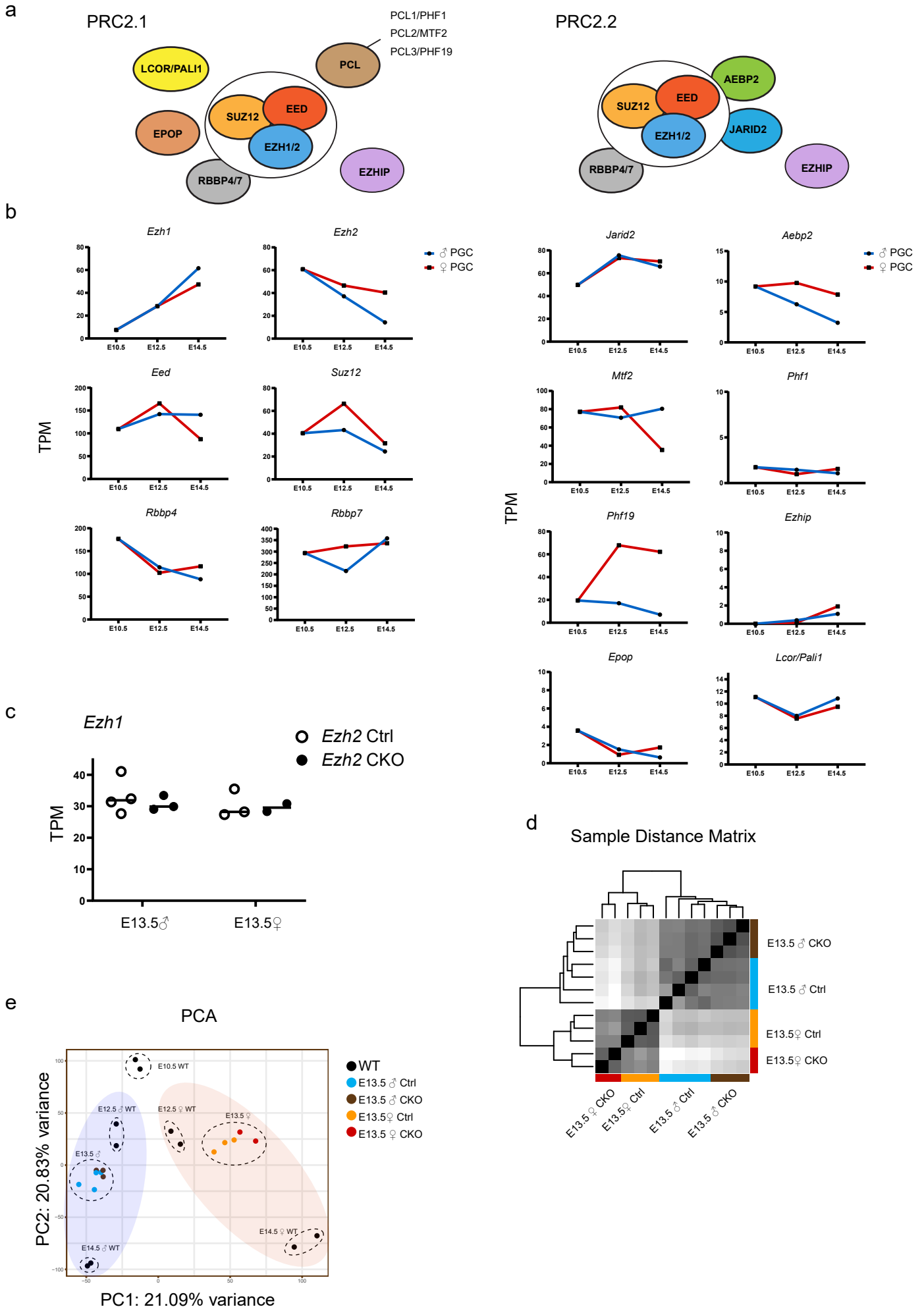
d



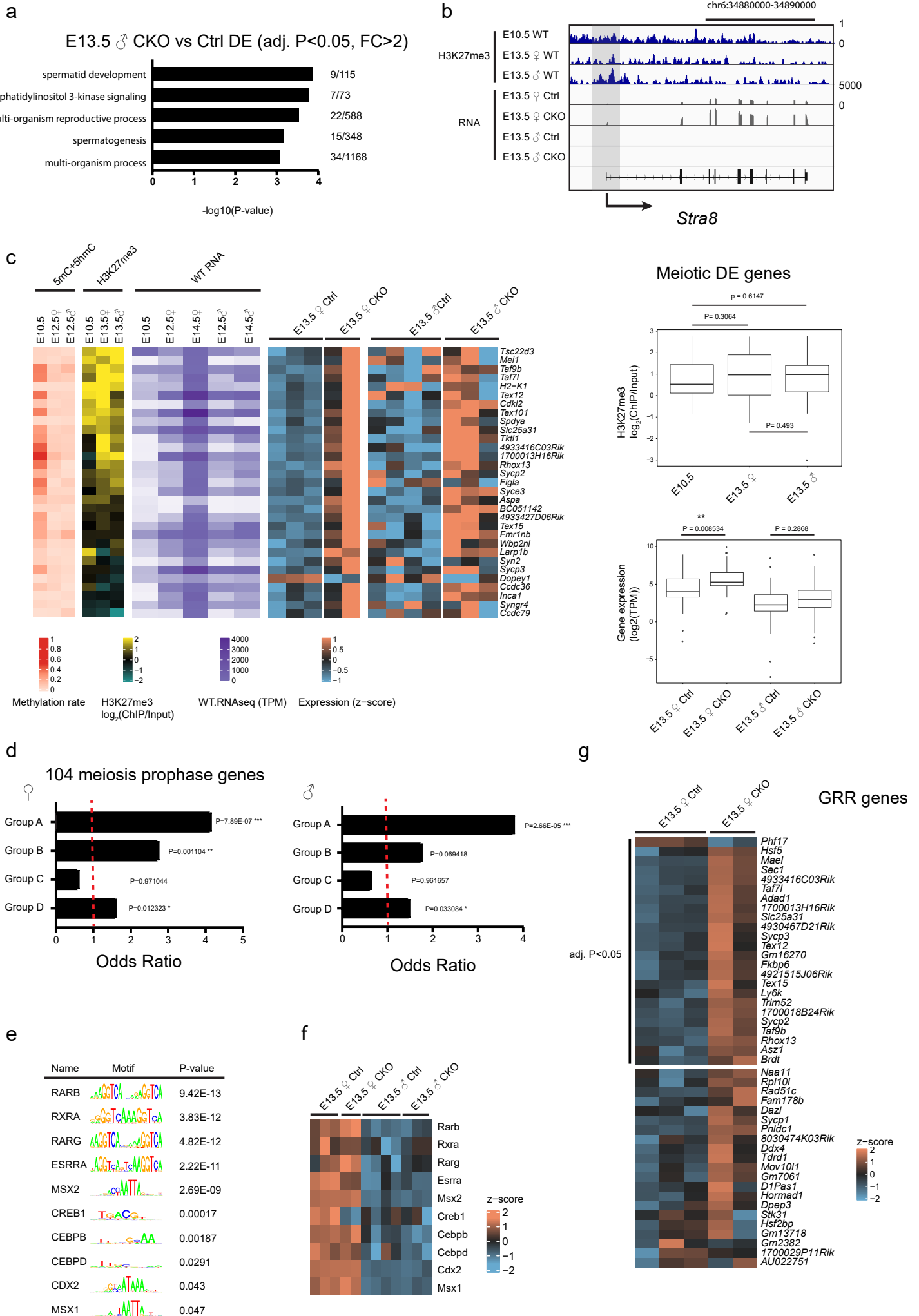
Extended Data Figure 5



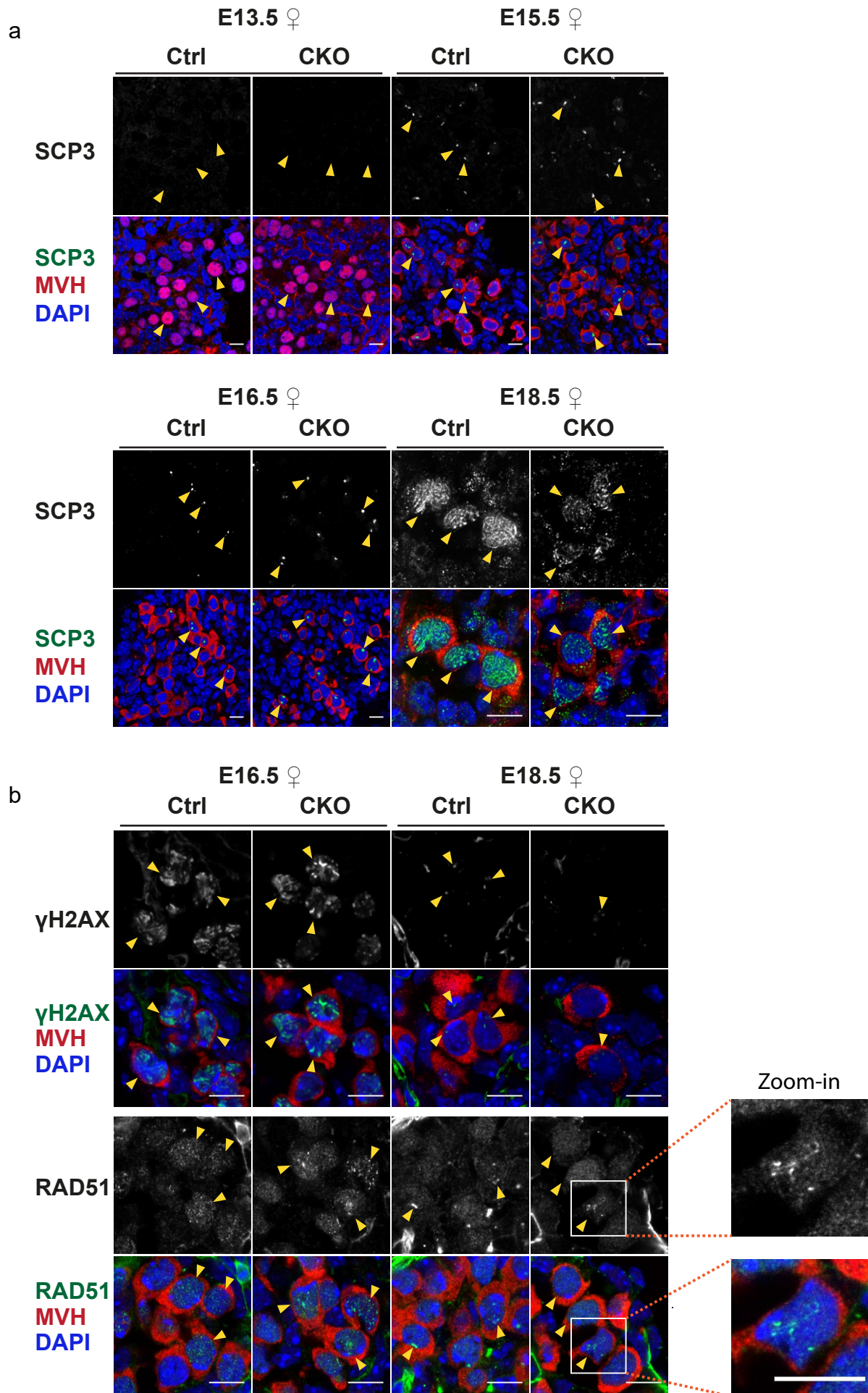
Extended Data Figure 6



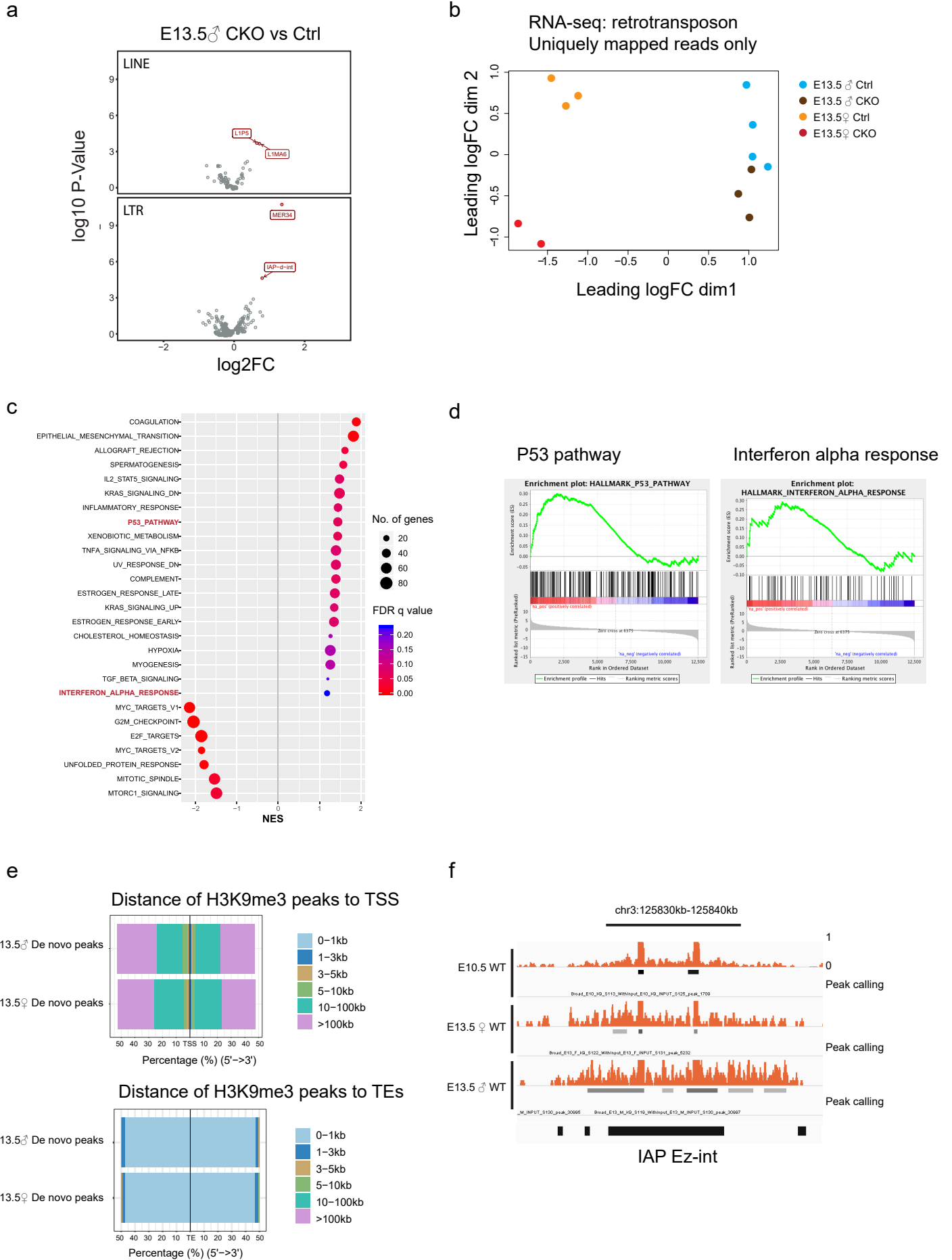
Extended Data Figure 7



Extended Data Figure 8



Extended Data Figure 9



Extended Data Figure 10

